A STUDY OF THE ^{2}H$(e, e'p)X$ REACTION AT LARGE 4-MOMENTUM TRANSFERS AND HIGH MISSING MOMENTA

A Thesis

Presented to

The Faculty of the Department of Physics and Astronomy

California State University, Los Angeles

In Partial Fulfillment

of the Requirements for the Degree

Master of Science

in

Physics

By

Shawn Love

May 2025

The thesis of Shawn Love is approved.

Dr. Konrad Aniol, Committee Chair

Dr. Jose Rodriguez, Committee Member

Dr. Radi Al-Jishi, Committee Member, Department Chair

California State University, Los Angeles

May 2025

ABSTRACT

A Study of the ^{2}H$(e, e'p)X$ Reaction at Large 4-Momentum Transfers and High Missing Momenta

By

Shawn Love

The short-range region ($r < 1$ fm) of the nucleon-nucleon potential may be studied via deuteron electro-disintegration. Such an experiment was done at Hall C of Jefferson Lab at 4-momentum transfers of $Q^2 = 4.07$ (GeV/c)^2 and reaching missing momenta up to 900 MeV/c. At such settings, complications arising from Meson Exchange Currents (MEC) and Isobar Currents are expected to be significantly minimized, as well as Final State Interactions (FSI) at recoiling angles of $\theta_{Xq} \sim 40°$. This makes comparisons of experimental and theoretical cross sections less model dependent.

A luminosity study was done to determine the reduction of liquid deuterium targets with increasing beam current. A 2.8% in the charge yield was found between 0 to 70 μA. Electron scattering from the walls of the target chamber was determined to be negligible, but caution was taken by considering scattering events away from the walls. A neutron was found to be contained in the missing mass spectrum for each missing momentum setting. Extraction of the deuteron total cross section is still on going.

ACKNOWLEDGMENTS

I would like to thank Dr. Konrad Aniol for his support throughout my time here at Cal State LA. I came into this program without any knowledge in nuclear or particle physics. I have learned so much and I'm excited to learn more within these fields.

I would like to thank our colleagues from Jefferson Lab: Dr. Carlos Yero, for his tremendous PhD thesis that has provided much information about this experiment; Dr. Mark Jones, for his assistance with wall scattering documentation; and Dr. Silviu Dusa for his fluid dynamics simulations. I would also like to thank PhD student Gema Villegas from Florida International University with her help in improving the database file, setting up weekly meetings, and providing Dr. Aniol and I with root files for us to analyze.

I would like to thank all of the friends I have made here at Cal State LA, who have given me their support throughout the Master Program. Special thanks to Erika Gwin for her tremendous assistance with the research project and her guidance in the Master Program.

Lastly, I would like to thank my girlfriend Danielle LaVine, who has given me continuous support and has provided assistance with statistical analysis.

TABLE OF CONTENTS

LIST OF TABLES

Table

LIST OF FIGURES

Figure

CHAPTER 1

Introduction

1.1 The Deuteron and Strong Nuclear Force

The *deuteron* (symbol ^{2}H or d) is the nucleus of the deuterium[1] atom and consists of a bound state of a neutron and a proton [5]. A summary of its properties is given in Table 1.1. Being the most simplest nucleon-nucleon (NN) bound state, the deuteron serves as a starting point in understanding the strong nuclear force (or NN-potential) [14], which is responsible for binding the quarks in hadrons[2], as well as binding protons and neutrons in atomic nuclei. [10]

Table 1.1. Properties of the deuteron. Note: Reprinted from [4].

Quantity	Value
Mass M_d	1875.612762 (75) MeV
Binding Energy ϵ	2.22456612 (48) MeV
Magnetic Dipole Moment μ_d	0.8574382284 (94) μ_N
Electric Quadrupole Moment Q_d	0.2859 (3) fm^2
Charge Radius r_{ch}	2.130 (10) fm
Matter Radius r_m	1.975 (3) fm
Electric Polarizability α_E	0.645 (54) fm^3

[1] Deuterium, also known as heavy hydrogen, is one of two stable isotopes of Hydrogen.

[2] A *hadron* is a bound state of two or more quarks. Hadrons made up of two quarks (one quark and one antiquark) are called *mesons*, while those made up of three quarks are called *baryons*.

Classically, interactions that occur over a distance, such as gravity and electromagnetism, are described in terms of a force field that is set up by a particle and which permeates all of space. This particle may then interact with any other particle via this field. In contrast, Quantum Field Theory (QFT) describes an "action at a distance" in terms of an *exchange interaction*, in which two particles interact with each other via the exchange of a particle that is associated with the particular type of interaction. The mediating particle carries momentum from one particle to the other, with the rate of change of momentum providing the force. In Quantum Electrodynamics (QED), the photon is the mediating particle for electromagnetic interactions. In Quantum Chromodynamics, the interquark force is mediated by the gluon. [10] While the effects of the exchanged particles are observable through the forces they mediate, they are not directly detectable. For this reason, they are often referred to as *virtual* particles.

The exchange interaction of the NN-potential depends on the internuclear separation distance r and may be subdivided into three regions (Fig. 1.1):

- the long-range region (LR), where $r > 2$ fm;
- the mid-range region (MR), where $1 < r < 2$ fm;
- the short-range region (SR), where $r < 1$ fm

The LR region is dominated by the exchange of a single pion, while the MR region is dominated by the exchange of two pions or by the exchange of heavier mesons. [9]

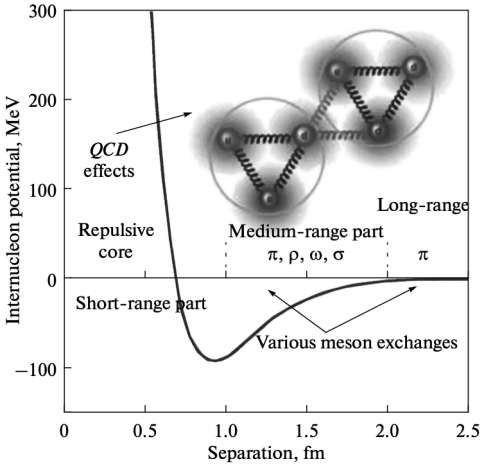

Figure 1.1. A qualitative plot of the NN-potential with separation distance. Note: Reprinted from Ref. [9].

The SR region, on the other hand, is the least understood theoretically and the most challenging to probe experimentally. At this region a very strong repulsive force is expected and can be explained by the Pauli exclusion principle, which forbids any two identical fermions from occupying the same quantum state. Given that quarks are fermions, as the proton and neutron begin to overlap, any three quarks in one nucleon must occupy higher energy states than those already filled by the three quarks in the other nucleon. This process requires significant energy which manifests as a strong repulsive force that resists bringing the two nucleons to sub-Fermi distances. By examining the structure of the deuteron in the SR region, one may determine at what point the description of the NN-potential in terms of nucleon-meson interactions are valid before having to take into account explicit quark effects. [14]

1.2 Electron Scattering Experiments

Having established that the SR region is of interest, we now inquire how to probe to such small distances experimentally. We recall that two objects can just be resolved as separate if their separation distance Δr is given by, for an optical microscope,

$$\Delta r \approx \lambda / \sin\theta, \tag{1.1}$$

where λ and θ are the wavelength and angular aperture, respectively, of the beam used to view the structure of an object. Resolving very small objects such as particles, then, requires having as short of a wavelength as possible. If the probing beam itself consists of pointlike particles, then the resolution is limited by the de Broglie wavelength of these particles,

$$\lambda = h/p, \tag{1.2}$$

where p is the beam momentum and h is Planck's constant. Thus, beams of high momentum (and therefore high energy) will have short wavelengths and can provide high resolution. [10]

As for the choice of particles making up the probing beam, electrons have proven to be the most valuable for a variety of reasons: they are lightweight and can be accelerated to extremely high speeds; their de Broglie wavelengths at high energies are very short; they can be finely controlled and focused using electric and magnetic fields; and their interactions are described by the well established theory of QED.

The use of electrons as a probing beam leads to electron scattering experiments, which remain one of the most valuable tools for particle physicists. We may classify such experiments into two types:

- **Inclusive:** In an inclusive electron scattering experiment, only the scattered electron is detected in the final state; no attempt is made to measure or identify other particles produced in the interaction. [14] These experiments focus on obtaining general information about the target structure, such as form factors or structure functions, which describe the distribution of charge and current in the target.
- **Exclusive:** In an exclusive electron scattering experiment, one or more particles are detected in-coincidence with the scattered electron. These experiments provide detailed information about specific interaction processes, such as the production of certain particles. [14]

Understanding the SR structure of the NN-potential requires us to know as much detailed information about the interaction as possible. Thus, an exclusive electron scattering experiment must be used.

1.3 Deuteron Electro-Disintegration

Subjecting the deuteron to an electron scattering experiment results in deuteron electro-disintegration:

$$e + d \rightarrow e' + p + n, \tag{1.3}$$

which we may write more compactly as $^2\mathrm{H}(e, e'p)n$. Using the exclusive electron scattering approach, one detects the scattered electron e' in-coincidence with the knocked-out proton p. The recoiled neutron n is not detected but instead is inferred from conservation laws.[3] Such experiments have been done since 1962 and serve as the most direct way of probing the internal structure of the deuteron. [14]

There are various interaction contributions that describe the reaction (1.3). These include the following (see [14]):

- **Plane Wave Impulse Approximation (PWIA):** The virtual photon couples directly to the bound proton, which is then ejected from the deuteron without any further interactions with the recoiling neutron.
- **Final State Interactions (FSI):** The ejected proton and recoiling neutron continue to interact further after being ejected from the deuteron, causing re-scattering of both nucleons.

[3]The reason for not detecting the neutron is due to its chargeless nature, making it notoriously difficult to detect.

- **Meson Exchange Currents (MEC):** The virtual photon couples to a virtual meson being exchanged between the two nucleons.
- **Isobar Currents (IC):** The virtual photon excites a bound nucleon, causing further re-scattering between the final state nucleons via the exchange of a pion.

Previous experiments (see [5] and [14]) have shown that under the appropriate conditions, FSI, MEC, and IC can be significantly reduced, leaving PWIA as the main contribution. This provides a much more favorable study of the short-range structure of the deuteron, as well as leaving theoretical descriptions less model-dependent. [14]

1.4 The General ^{2}H$(e, e'p)X$ Reaction Kinematics

Probing the SR region of the deuteron requires electron beam energies in the GeV range. The binding energy[4] of the deuteron, however, is only a mere 2.22 MeV. Since the incoming electrons will have energies much larger than the deuteron binding energy, it is possible that there will be other particles not detected along with the neutron. To take into account our inability to detect all possible particles that may arise from this reaction, we consider the more general reaction ^{2}H$(e, e'p)X$, where X can be any particle or any system of particles; that is,

$$e + d \rightarrow e' + p + X. \tag{1.4}$$

[4]The *binding energy* of a nucleus is the minimum energy required to break apart the nucleus into its constituent nucleons.

In particle physics, particles that are not detected are referred to as "missing" and are labeled as X. We say that X has "missing momentum" $\mathbf{p}_X$ and "missing energy" E_X. We rely on measurements of the detected particles and on conservation laws to infer what particle X is. In our present case, we expect X to either be a neutron or to at least contain a neutron. This of course would need to be confirmed with the appropriate measurements and calculations to be discussed below. Note that we shall employ natural units in our discussion: $\hbar = c = 1$.

The kinematics for the general $^2\mathrm{H}(e, e'p)X$ reaction under PWIA and using the One Photon Exchange Approximation (OPEA) is shown in Fig. 1.2. In the scattering plane, an incoming electron e exchanges a virtual photon γ and is then scattered e'. The virtual photon γ then interacts with the deuteron in the reaction plane, causing the deuteron to be broken up into a proton p and to X.

The electron's initial and final four-momentum are $P_e^\mu = (E, \mathbf{k})$ and $P_{e'}^\mu = (E', \mathbf{k}')$, respectively. By applying conservation of four-momentum at the electron vertex, we find the four-momentum q_γ^μ of the exchanged virtual photon to be

$$P_e^\mu = P_{e'}^\mu + q_\gamma^\mu \quad \Longrightarrow \quad q_\gamma^\mu \equiv P_e^\mu - P_{e'}^\mu = (E - E', \mathbf{k} - \mathbf{k}') = (\omega, \mathbf{q}) \tag{1.5}$$

where $\omega = E - E'$ is the energy change and $\mathbf{q} = \mathbf{k} - \mathbf{k}'$ is the change in three-momentum. The four-momentum transfer of the virtual photon is expressed conveniently as the Lorentz invariant

$$Q^2 \equiv -q^\mu q_\mu = q^2 - \omega^2 = (\mathbf{k} - \mathbf{k}')^2 - (E - E')^2, \tag{1.6}$$

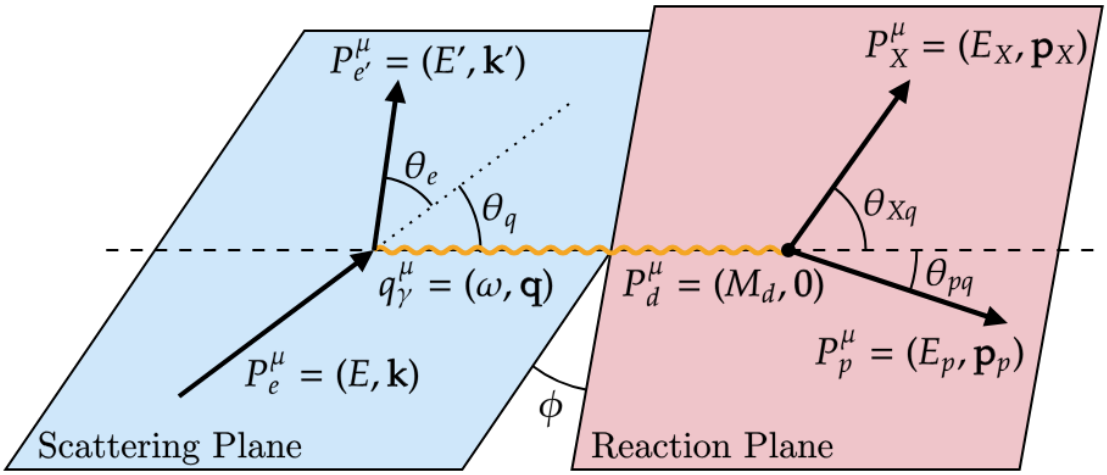

Figure 1.2. Feynman diagram of the general $^2\mathrm{H}(e, e'p)X$ reaction kinematics under the One-Photon Exchange Approximation. Note: Redrawn from Ref. [14]

or in expanded form,

$$Q^2 = k^2 + k'^2 - 2\mathbf{k}\cdot\mathbf{k}' - E^2 - E'^2 + 2EE'. \tag{1.7}$$

In the extreme relativistic limit (ERL), the electron mass m_e is negligible and we may make the approximation that $E \approx k$ and $E' \approx k'$ [5]. Furthermore the angle between $\mathbf{k}$ and $\mathbf{k}'$ is θ_e, the scattering angle of the electron. This reduces Eq. (1.7) to

$$Q^2 = 2kk'(1 - \cos\theta_e) = 4kk'\sin^2\left(\frac{\theta_e}{2}\right). \tag{1.8}$$

Since the deuteron is taken to be at rest in the lab frame, the four-momentum of the deuteron with mass M_d is $P^\mu_d = (M_d, \mathbf{0})$. The final state proton and X have four-momentum $P^\mu_p = (E_p, \mathbf{p}_p)$ and $P^\mu_X = (E_X, \mathbf{p}_X)$, respectively. Applying conserva-

tion of four-momentum at the hadron vertex yields

$$q^\mu_\gamma + P^\mu_d = P^\mu_p + P^\mu_X \quad \Longrightarrow \quad (\omega, \mathbf{q}) + (M_d, \mathbf{0}) = (E_p, \mathbf{p}_p) + (E_X, \mathbf{p}_X). \tag{1.9}$$

From momentum conservation of Eq. (1.9), we obtain expressions for the missing momentum and final proton momentum:

$$\mathbf{p}_p = \mathbf{q} - \mathbf{p}_X, \tag{1.10}$$

$$\mathbf{p}_X = \mathbf{q} - \mathbf{p}_p. \tag{1.11}$$

Squaring both sides of each equation yields

$$p_p^2 = q^2 + p_X^2 - 2qp_X \cos\theta_{Xq}, \tag{1.12}$$

$$p_X^2 = q^2 + p_p^2 - 2qp_p \cos\theta_{pq}, \tag{1.13}$$

where θ_{Xq} is the angle between $\mathbf{q}$ and the final momentum $\mathbf{p}_X$ of particle X, and θ_{pq} is the angle between $\mathbf{q}$ and the final momentum $\mathbf{p}_p$ of the proton. Substituting Eq. (1.13) into Eq. (1.12) and solving for $\cos\theta_{Xq}$ yields

$$\cos\theta_{Xq} = \frac{q - p_p \cos\theta_{pq}}{\sqrt{q^2 + p_p^2 - 2qp_p \cos\theta_{pq}}}. \tag{1.14}$$

From energy conservation of Eq. (1.9), we find the missing energy to be

$$E_X = \omega + M_d - E_p. \tag{1.15}$$

Using the relation $E = \sqrt{m^2 + \mathbf{p}^2}$, a calculation of the observables E_X and $\mathbf{p}_X$ allows one to determine the mass of X:

$$m_X = \sqrt{E_X^2 - \mathbf{p}_X^2} = \sqrt{(\omega + M_d - E_p)^2 - (q^2 + p_p^2 - 2qp_p \cos\theta_{pq})^2}. \tag{1.16}$$

We expect the neutron to be contained within this missing mass.

Previous $^2\mathrm{H}(e,e'p)n$ experiments (see [5] and [14]) have shown that at large four-momentum transfers Q^2 (> 1 GeV^2) and high missing momentum $\mathbf{p}_X$, contributions from MEC and IC are significantly reduced. Furthermore, at these settings FSI is also significantly reduced at angles $\theta_{Xq} \sim 40^\circ$. This leaves PWIA as the main contribution, meaning that the interaction described by the Feynman Diagram in Fig. 1.2 and the subsequent calculations made from it are valid.

1.5 The Interaction Cross Section

The fundamental physics of any scattering experiment is contained in the so-called *cross section* σ. As we shall see, it is useful to think of the cross section as the *effective* cross-sectional area associated with each target particle. In the case of the $^2\mathrm{H}(e,e'p)X$ reaction, a calculation of the cross section would refer to the effective cross-sectional area of the deuteron. In general, however, the cross section gives the quantum mechanical probability that an interaction will occur. [13]

1.5.1 Experimental Cross Sections

We motivate the definition of the cross section by the classical picture shown in Fig. 1.3a, in which a beam of projectiles with cross-sectional area A_b are to be made incident onto a target chamber of thickness ΔL ([L]) and containing targets of density n_t (number/volume, $[\mathrm{L}]^{-3}$). For now, let us just focus our attention to a single

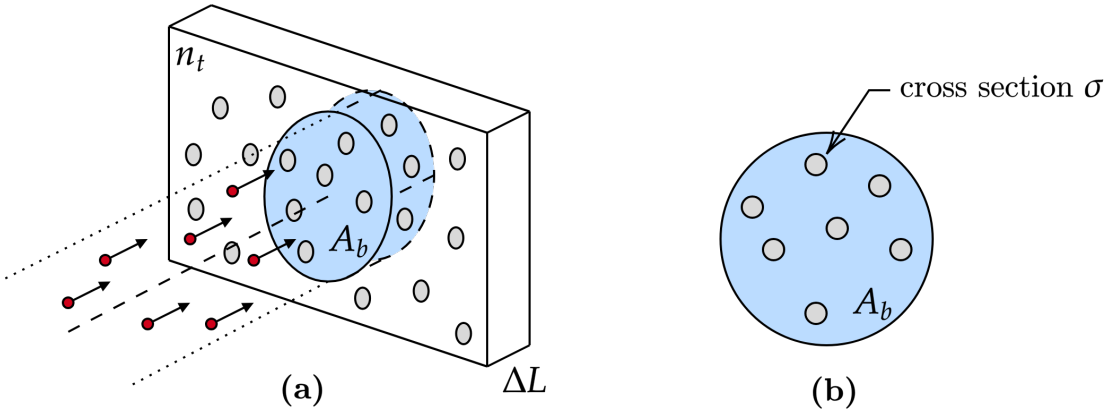

Figure 1.3. Classical cross section diagram. **(a)** A beam of projectiles with cross-sectional area A_b incident onto a target chamber. **(b)** The assembly of targets as seen by an incoming projectile. The cross section σ is the area of any one target, perpendicular to the incident direction.

projectile. Since we do not know the projectile's precise trajectory, we cannot say with certainty whether it will hit any of the targets or how many it will hit. However, we can calculate the *probability* that it will make a hit in the following way. [12] The projectiles making up the beam can only hit the targets that are within the beam's path. The number of targets N_t that are in this path is given by

$$N_t = n_t V_b = n_t A_b \Delta L, \tag{1.17}$$

where $V_b = A_b \Delta L$ is the volume of the beam's path inside the target chamber.

Let σ be the cross-sectional area, or simply the **cross section**, of each target as seen from the incoming projectile, as shown in Fig. 1.3b. Now the total cross-sectional area occupied by the targets within the beam's path is given by $N_t\sigma$. Therefore, the probability that any one projectile makes a hit as it passes through the target chamber is given by the ratio

$$\begin{aligned} P(\text{hit}) &= \frac{\text{total area occupied by targets within beam area}}{\text{beam area}} = \frac{N_t\sigma}{A_b} = \frac{n_t A_b \Delta L \sigma}{A_b} \\ &= n_t \Delta L \sigma. \end{aligned} \tag{1.18}$$

If we multiply this probability by the total number of incident projectiles N_{inc}, we then obtain the total number of scattered projectiles N_{sct}:

$$N_{\text{sct}} = P(\text{hit}) \cdot N_{\text{inc}} = N_{\text{inc}} n_t \Delta L \sigma. \tag{1.19}$$

In practice one uses a steady of stream of particles and it is more convenient to consider the *rate* of incident particles and the rate of scattered particles. Dividing

both sides by dt gives

$$\Gamma_{\text{sct}} = \Gamma_{\text{inc}} n_t \Delta L \sigma. \tag{1.20}$$

It is further convenient to define the **luminosity** as

$$\mathcal{L} \equiv \Gamma_{\text{inc}} n_t \Delta L. \tag{1.21}$$

This is a very important parameter of any particle accelerator; it measures how many particle collisions occur per unit time and area, essentially quantifying the rate at which particles are brought together to collide. With this definition, the cross section may be expressed in its simplest form as

$$\sigma = \frac{\Gamma_{\text{sct}}}{\mathcal{L}}. \tag{1.22}$$

We see that the cross section is a constant of proportionality between the luminosity and reaction rate. [14] This result is often called the *total* cross section. In general, the scattering rate is not as simple as the expression given in Eq. (1.20); it is a rather involved calculation that requires the rigorousness of scattering theory in quantum mechanics (Fermi's golden rule, etc.).

The cross section given in Eq. (4.1) gives the overall probability that a particle will scatter. However, it does not tell us anything about how it scatters—whether it prefers certain angles or energy changes. In many cases, the distribution of some kinematic variable is also of importance. In particular, knowing the angular distribution of the scattering particles provides more detailed information about the fundamental

physics of the interaction. [13] To this end, the relevant parameter is the *differential* cross section for the scattering rate into an element of solid angle $\mathrm{d}\Omega = \sin\theta\,\mathrm{d}\theta\,\mathrm{d}\phi$:

$$\frac{\mathrm{d}\sigma}{\mathrm{d}\Omega} = \frac{\text{number of particles scattered into } \mathrm{d}\Omega \text{ per unit time per target particle}}{\text{luminosity}}. \tag{1.23}$$

The total cross section is then found via integration:

$$\sigma = \int \frac{\mathrm{d}\sigma}{\mathrm{d}\Omega}\,\mathrm{d}\Omega\,. \tag{1.24}$$

Another kinematic variable of interest is the energy distribution of the scattered particle. We may then have a differential cross section of the form

$$\frac{\mathrm{d}\sigma}{\mathrm{d}E} = \frac{\text{number of particles scattered with energy } \mathrm{d}E \text{ per unit time per target particle}}{\text{luminosity}}. \tag{1.25}$$

Going one step further, we may even consider the joint angular and energy distribution of scattered particles to obtain even more detailed information about the interaction. In our present case for the deuteron electro-disintegration, the kinematic variables of interest are the angular distributions of the scattered electron and scattered proton, as well as the energy distribution of the electron (see Fig. 1.4). We therefore wish to obtain a cross section of the form

$$\sigma = \int \frac{\mathrm{d}^5\sigma}{\mathrm{d}\Omega_e\,\mathrm{d}\Omega_p\,\mathrm{d}E_e}\,\mathrm{d}\Omega_e\,\mathrm{d}\Omega_p\,\mathrm{d}E_e\,. \tag{1.26}$$

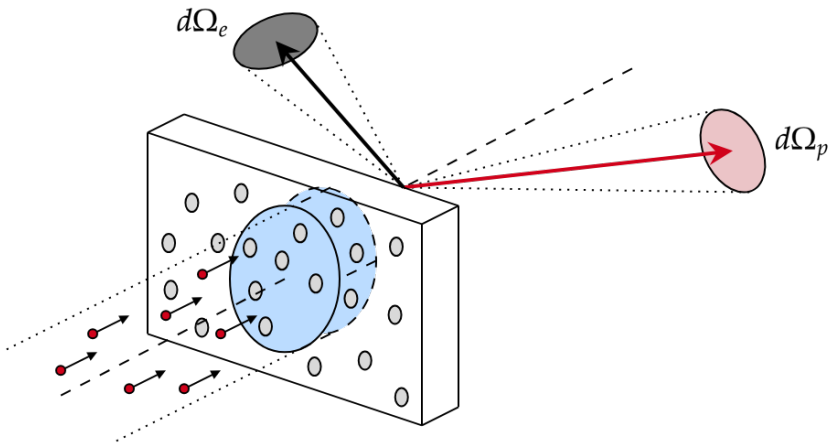

Figure 1.4. Angular distribution of scattered electron $\mathrm{d}\Omega_e$ and scattered proton $\mathrm{d}\Omega_e$.

1.5.2 Theoretical Cross Sections

Various theoretical groups have determined phenomenological models of the NN-potential using different techniques in their approach. From these modeled NN-potentials, one may then obtain a theoretical cross section by first solving the Schrodinger equation

$$\hat{H}_d\psi_d(\mathbf{r}) = E_d\psi_d(\mathbf{r}) \quad \Longrightarrow \quad \left(\hat{T}_p + \hat{T}_n + \hat{V}_{nn}\right)\psi_d(\mathbf{r}) = E_d\psi_d(\mathbf{r}), \tag{1.27}$$

where $\hat{H}_d$ is the Hamiltonian operator that acts on the deuteron wave function $\psi_d(\mathbf{r})$. The Hamiltonian is expressed in terms of the kinetic energy operators of the proton and neutron, $\hat{T}_p$ and $\hat{T}_n$, respectively, as well as the modeled NN-potential $\hat{V}_{nn}$. By using Eq. (1.27) to solve for the deuteron wave function, one may then determine the

scattering amplitude, from which the theoretical cross section can then be calculated and compared with the experimentally determined cross section.

1.6 Experiment E12-10-003

Experiment E12-10-003 was taken in Hall C at Jefferson Laboratory from February 24th, 2023 through March 20th, 2023. The goal of this experiment is to systematically explore the $^2\mathrm{H}(e, e'p)X$ reaction at large four-momentum transfers and large missing momentum for a favorably study of the short range structure of the deuteron, thereby providing more information about the NN-potential. Furthermore, extracting the cross section of this reaction allows one to compare with that of theoretical models. This experiment extends the previous Hall A [2] and Hall C [14] measurements of the $^2\mathrm{H}(e, e'p)X$ cross section.

CHAPTER 2

Experimental Setup

2.1 Electron Beam for Scattering Experiments

Electron scattering experiments, such as the deuteron electro-disintegration experiment, are done at Jefferson Lab with the use of their Continuous[1] Electron Beam Accelerator Facility (CEBAF). This particle accelerator employs superconducting radiofrequency (SRF) to accelerate electrons. A schematic of the CEBAF with the recent 12 GeV upgrade is shown in Fig. 2.1.

The CEBAF process begins with the injector, which generates the electron beam by shining a laser into a GaAs photocathode. The beam is then accelerated up to 123 MeV before entering the cryomodules of the North Linac. Each cyromodule contains 8 7-cell SRF resonant cavities that are excited at frequency of $f_0 = 1497$ MHz, resulting in electric fields that alternate in each cell. In order to accelerate the electrons, the electric fields are reversed in periodic cycles of $T = 1/f_0$ such that by the time the electrons have reached the end of one cell, they can then be accelerated by the next cell, and so forth (see Fig. 2.2). After traversing through the North Linac, the beam has received a 1.1 GeV gain in energy. The beam is then steered via

[1] Although the electron beam is considered to be a continuous beam, it is really a pulsed beam with a frequency given by the injector laser.

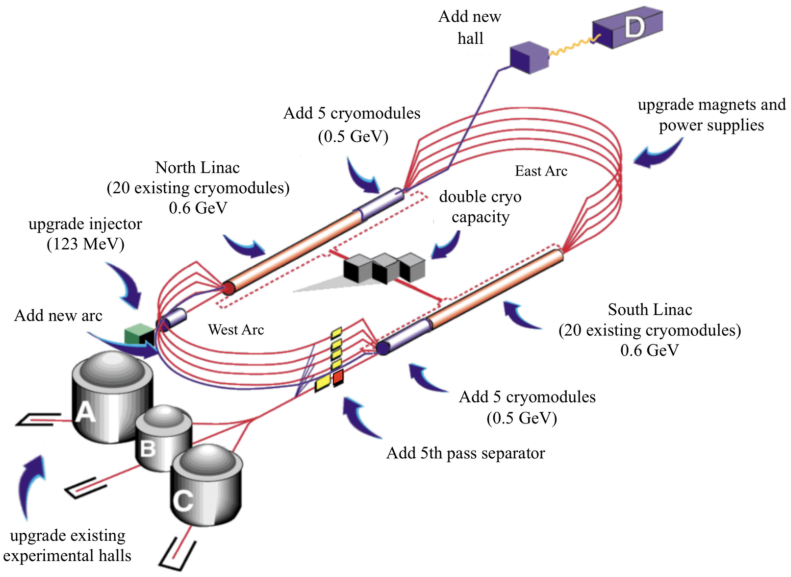

Figure 2.1. Schematic of the CEBAF at Jefferson Lab after the 12 GeV upgrade. Note: Reprinted from Ref. [14].

magnets into the East Arc and sent into the South Linac for an additional 1.1 GeV gain in energy. At this point, the beam has finished a single pass and has a beam energy of 2.2 GeV; any additional pass will give the beam an additional 2.2 GeV of energy. It is up to the physics demands of a particular experiment to decide how many passes the beam should receive, up to a total energy beam of 12.1 GeV. Once the desired beam energy has been obtained, the beam is then set to a separator that sends the beam into the appropriate experimental hall. [14]

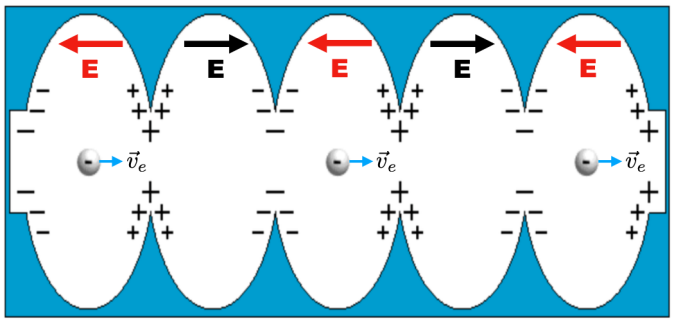

Figure 2.2. Oscillating electric fields in the SRF resonant cavity. Note: Reprinted from Ref. [14].

2.2 Targets and Target Chamber

Once the electron beam has the acquired the desired energy, it is sent to the respective experimental hall to which it presents itself onto the target chamber. The target chamber in Hall C is a large evacuated aluminum tank kept at a pressure of 10^{-6} torr via a vacuum pump. The entrance windows of the Hall C spectrometers are very close to, but not in direct contact with the target chamber window. Thus, the scattered particles pass through the exit windows of the target chamber, travel a short distance in the air, and then enter the spectrometer by passing through the spectrometer's entrance window (see Fig. 2.7). [14]

The targets themselves are kept in a target ladder that is housed inside the target chamber. The target ladder is capable of holding solid targets and cryogenic targets, that is, targets that are kept at very low temperatures (≈ 20 K). These targets

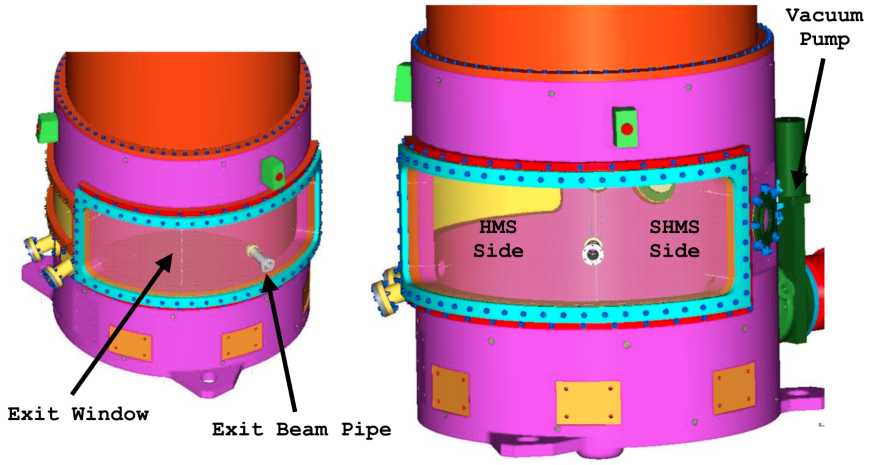

Figure 2.3. CAD drawing of the Hall C Target Chamber. Note: Reprinted from [14].

are typically Hydrogen and Deuterium gas that are cooled into a liquid state via the coolant supply from the End-Station Refrigerator (ESR). To keep the cryogenic targets at very low temperatures, they are constantly recirculated via a heat exchanger (see Fig. 2.4). The electron beam interacts only with the the cryogenic targets that are inside the target cell, which is 10 cm long. [14]

2.3 Hall C Spectrometers

The main equipment used in Hall C to study particle interactions and obtain high-precession cross-section measurements are the High Momentum Spectrometer (HMS) and Super High Momentum Spectrometer (SHMS). [14] The purpose of these spectrometers are to transport the scattered particles from the target chamber into their respective particle detectors. Each spectrometer is set to have a certain central mo-

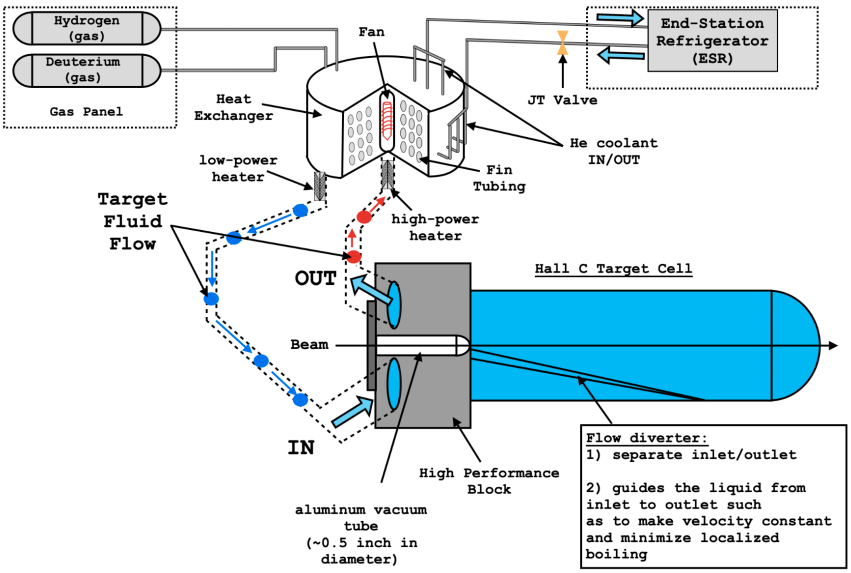

Figure 2.4. Recirculation of cryogenic targets via a heat exchanger. Note: Reprinted from [14].

mentum and central angle value, meaning that only the scattered particles that are within the spectrometer's central momentum/angle are to be detected. It is up to the physics demands of a particular experiment to determine what central momentum/angle should be set to the spectrometers. The demonstrated performance and design specifications of each spectrometer is given in Table 2.1.

2.3.1 Spectrometer Slit System

As the electron beam interacts with the target atoms, the final-state particles can scatter in all sorts of directions. A slit system is placed into each spectrometer to select only the scattered particles that are within the spectrometer's central momentum and

Table 2.1. Demonstrated Performance and Design Specifications of the HMS and SHMS. Note: Reprinted from [14].

Parameter	**HMS Performance**	**SHMS Specification**
Range of Central Momentum	0.4 to 7.4 GeV/c	2 to 11 GeV/c
Momentum Acceptance	$\pm 10\%$	-10% to $+22\%$
Momentum Resolution	$0.1\% - 0.15\%$	$0.03\% - 0.08\%$
Scattering Angle Range	10.5° to 90°	5.5° to 40°
Target Length Accepted at 90°	10 cm	50 cm
Horizontal Angle Acceptance	± 32 mrad	± 18 mrad
Vertical Angle Acceptance	± 85 mrad	± 50 mrad
Solid Angle Acceptance	8.1 msr	> 4 msr
Horizontal Angle Resolution	0.8 mrad	0.5 - 1.2 mrad
Vertical Angle Resolution	1.0 mrad	0.3 - 1.1 mrad
Target Resolution (ytar)	0.3 cm	0.1 - 0.3 cm
Maximum Event Rate	2000 Hz	10,000 Hz
Maximum Flux within Acceptance	~ 5 MHz	~ 5 MHz
e/h Discrimination	$> 1000:1$ at 98% efficiency	$> 1000:1$ at 98% efficiency
π/K Discrimination	100:1 at 95% efficiency	100:1 at 95% efficiency

angular acceptance setting. [14]

2.3.2 Spectrometer Magnets

Each spectrometer is equipped with superconducting magnets that guide the scattered particles into the spectrometer's respective detector stack (see Fig. 2.5). Specifically, the three quadrupole magnets (Q) in each spectrometer focuses the scattered particles into the dipole magnet (D), which then bends the scattered particles onto a focal plane inside the detector stack. The SHMS has an additional dipole magnet (d) known as the Horizontal Bender, which serves to bend and detect particles at certain angles that would have otherwise been obstructed by the first quadrupole magnet. To set the spectrometers central momentum, a field setting program is used to select the appropriate magnetic field for each magnet. [14]

2.3.3 Spectrometer Detectors

In particle physics, any particle collision or interaction is known as an *event*. In this experiment, we are interested only in the events corresponding to the $^2\mathrm{H}(e, e'p)X$ interaction. This is achieved by using various particle detectors, each of which using various technologies to detect, identify, and measure particles produced in high-energy collisions. [13] The goal is to trace the signals from the various detector systems back to the Feynman diagram responsible for the $^2\mathrm{H}(e, e'p)X$ interaction.

Both spectrometers are equipped with a similar set of particle detectors that

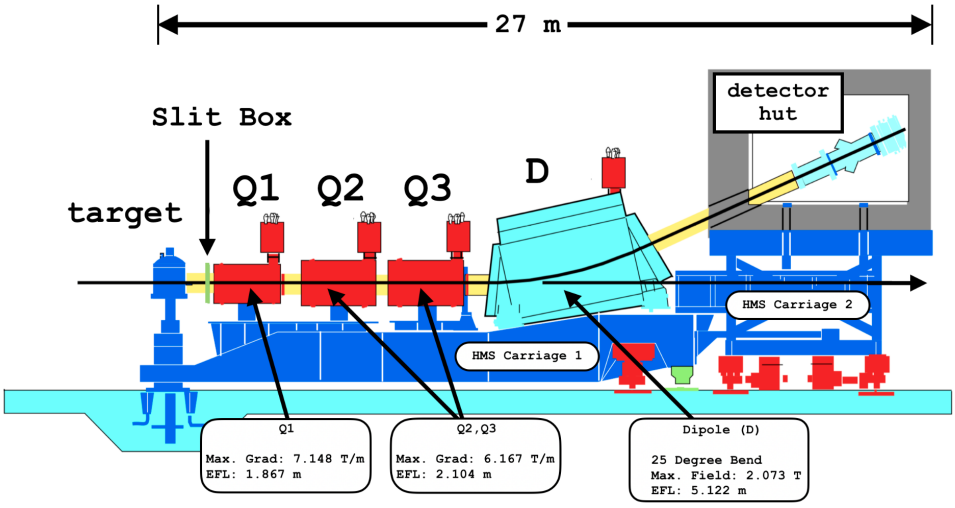

(a) High Momentum Spectrometer (HMS) side view.

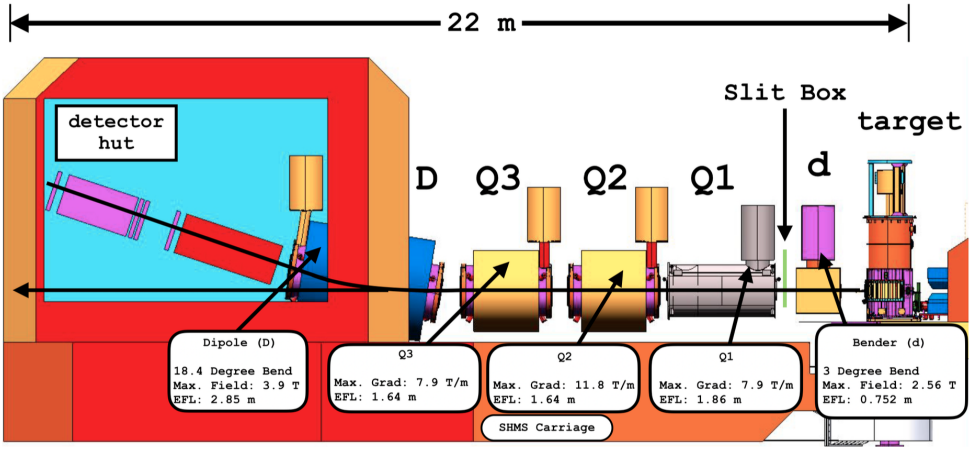

(b) Super High Momentum Spectrometer (SHMS) side view.

Figure 2.5. Side view of the Hall C spectrometers. Note: Reprinted from [14]

are housed in a heavily shielded container known as the detector hut, as shown in Fig. 2.6. The detector system consists of drift chambers used for track reconstruction, hodoscope planes used for particle triggering, a calorimeter used for e/π separation, and Cherenkov detectors for additional particle identification. [14]

Drift Chambers

Each spectrometer is equipped with two drift chambers, each of which consisting of 6 anode wire planes and 8 cathode planes. The two drift chambers are separated by a focal plane, where the origin of this focal plane coincides with the focal point of the spectrometer optics. Thus, particles that enter the hut are focused on this focal plane, and those with a momentum equal to the central momentum of the spectrometer are focused at the origin. A side view of two drift chambers is shown in Fig. 2.7. [14]

Each wire plane consists of alternating field wires and sense wires. The HMS drift chamber consists of 96 sense wires in the U, U', V, V' planes, and 102 sense wires in the X, X' planes. The SHMS drift chamber consists of 107 sense wires in the U, U', V, V' planes, and 79 sense wires in the X, X' planes. The field wires and cathode planes are kept at a negative potential while the sense wires are grounded, resulting in a potential gradient that creates an electric field oriented outwards from the sense wires. Each chamber is filled with a gas mixture consisting of 50:50 argon/ethane. As a charged particle traverses the drift chambers, it ionizes the gas atoms. The free electrons from the ionized gas are then drifted towards sense wires via the electric field

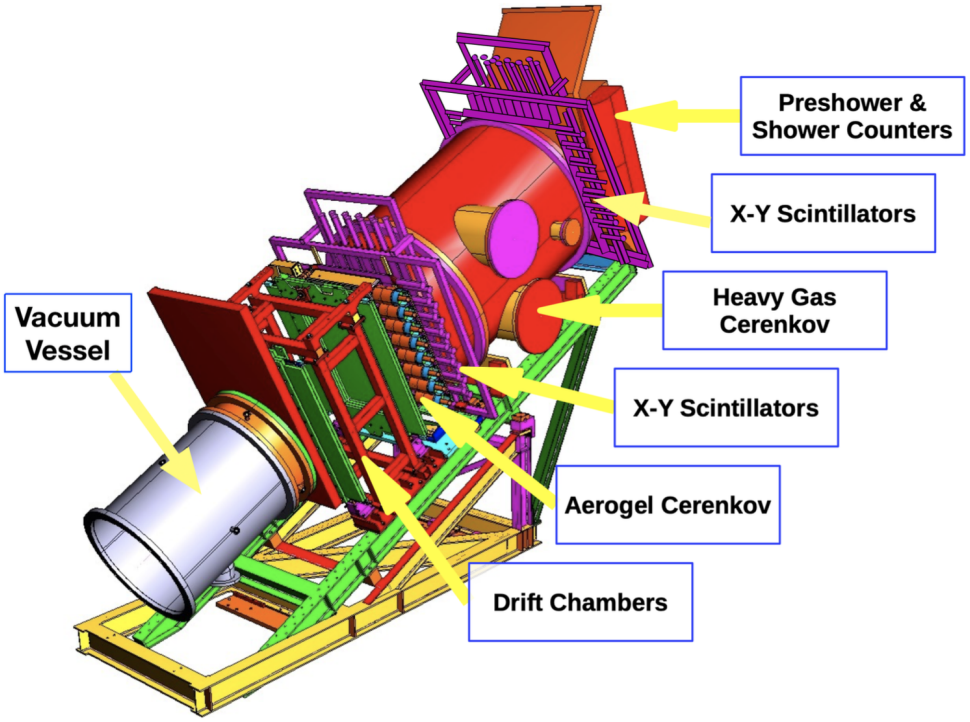

(a) High Momentum Spectrometer (HMS) detector stack.

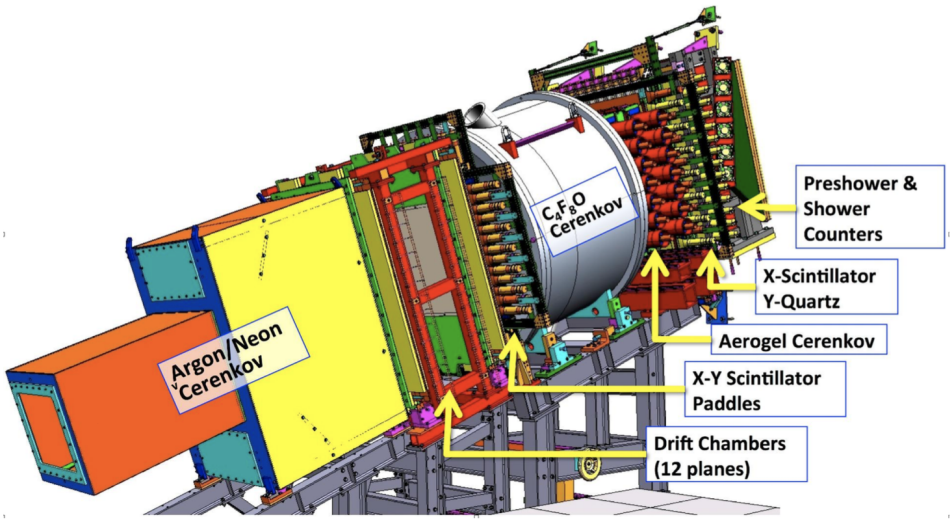

(b) Super High Momentum Spectrometer (SHMS) detector stack.

Figure 2.6. Hall C detector stacks. Note: Reprinted from [14]

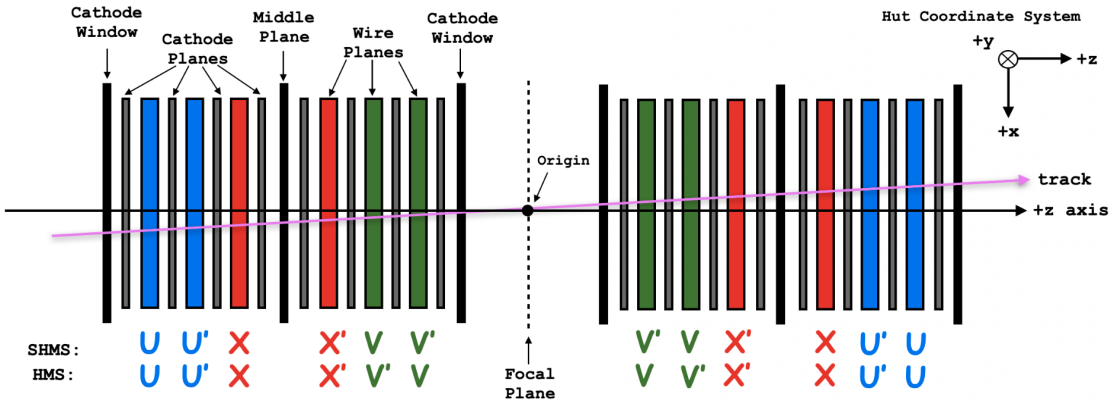

Figure 2.7. Side view of the two drift chambers in the HMS and SHMS. The focal plane is where particles are focused as they enter the hut; particles with the same momentum as the central spectrometer momentum are focused at the origin. Note: Reprinted from [14].

from the potential gradient (see Fig. 2.8). This produces a measurable current signal that can be used to determine the *drift time*, that is, the time it took the each electron to drift towards a sense wire. [14] The drift time can then be used to determine the drift distance of each ionized electron, thereby allowing one to reconstruct the charged particle's path and momentum.

Ideally, the drift chamber should appear early in the detection system so that it can reconstruct the particle's trajectory and momentum immediately after the collision. In the SHMS, the drift chambers are placed after th Noble Gas Cherenkov detectors due to space constraints. [14]

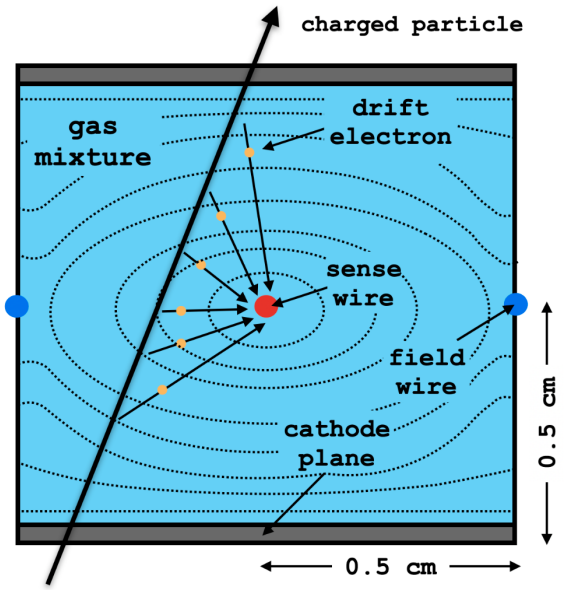

Figure 2.8. Trajectory of a charged particle in a drift chamber cell. Note: Reprinted from [14].

Hodoscope Detectors

Each spectrometer is equipped with hodoscope planes, which consists of a series of scintillator arrays segmented along the x-axis and y-axis. The scintillators are coupled with a photomultiplier tube (PMT) at each end. As a charged particle traverses this detector, it excites the molecules in the scintillator material. These excited molecules then decay back into the ground state via the emission of photons, which then propagate through the scintillator until they are detected by the PMT. As the photons interact with the PMT photocathode, electrons in the material begin to escape via the photoelectric effect. These electrons then produce a measurable analog signal that is sent to the Counting Room for signal processing and data collection (see Fig. 2.9).

The fast timing properties of scintillators allows for ideal particle triggering. In high energy physics, a trigger is a system that uses a selection criteria to rapidly decide which events to keep. [8] This reduces the amount of data to be taken, as data storage can present a problem in terms of costs and space. In this case, the triggering system has been set up such that only events that have fired at least 3 of the 4 hodoscope planes are selected (i.e., only these data are stored). [14]

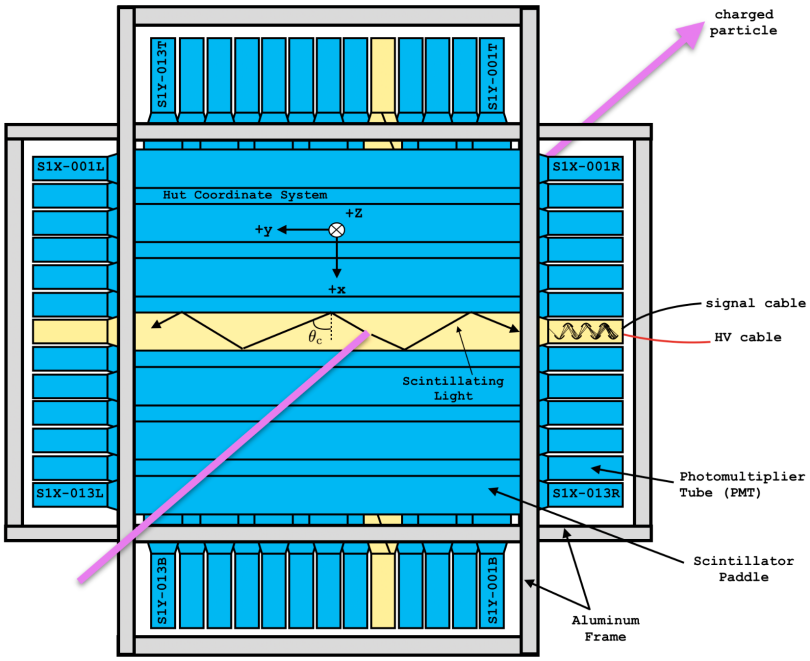

Figure 2.9. A pair of hodoscope planes in the SHMS. Note: Reprinted from [14].

Cherenkov Detectors

Cherenkov radiation occurs when a charged particle traverses a medium faster than the speed of light in that medium. This polarizes the medium in such a way that photons are emitted and distributed in a conical shape about the trajectory of the particle. The geometry of this radiation, which is analogous to that of a sonic boom for sound waves, is shown in Fig. 2.10. In time t, the particle travels a distance

$$d = vt = \beta ct, \tag{2.1}$$

where $\beta = c/v$ is the ratio of the velocity v of the charged particle to the speed of light c in vacuum. In this time, the wavefront emitted at $t = 0$ has traveled a distance

$$r = ut = ct/n, \tag{2.2}$$

where $u = c/n$ is the ratio of the speed of light c in vacuum to the index of refraction n of the medium; that is, u is the speed of light in the medium. Thus, the angle at which Cherenkov radiation is produced is given by

$$\cos\theta = \frac{1}{n\beta}. \tag{2.3}$$

Cherenkov radiation is emitted only when $v > u$, or, equivalently, $\beta > 1/n$. From the relation $\beta = pc/E = p/\sqrt{m^2 + p^2}$, we may write this inequality in terms of the particle's mass m and momentum p:

$$n > \frac{\sqrt{m^2 + p^2}}{p}. \tag{2.4}$$

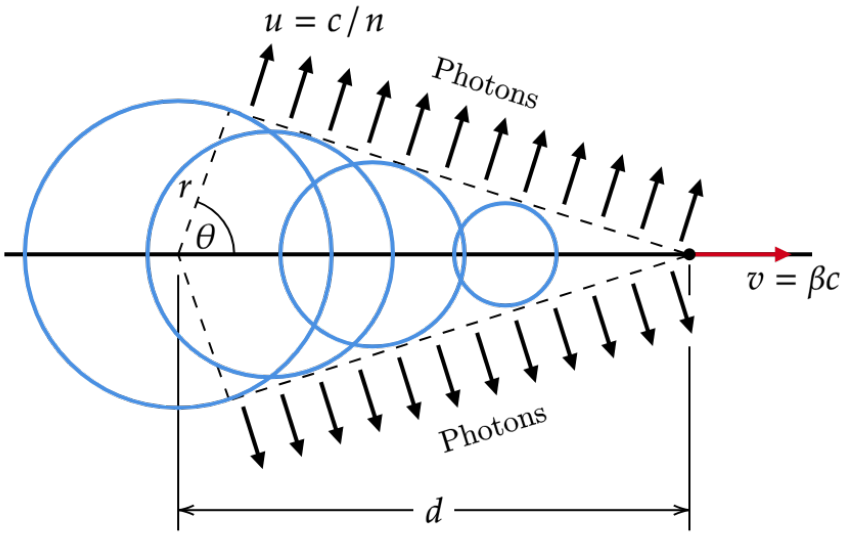

Figure 2.10. The geometry of Cherenkov radiation.

For a particle with a fixed momentum and a medium with a given index of refraction, the mass of the particle will determine whether Cherenkov radiation will be produced. Therefore, a suitable choice for the medium may be utilized to aid the identification of particles. To this end, the Hall C spectrometers are equipped with the following threshold Cherenkov detectors (see [14]):

- **Heavy Gas Cherenkov (HGC):** Both spectrometers are equipped with an HGC detector that uses a certain gas for particle identification. The HMS HGC detector may use either C_4F_10 or N_2 gas to distinguish between e/π, or may use Freon-12 gas to distinguish between π/p. The SHMS HGC detector uses C_4F_8O gas to distinguish between e/π or π/K, depending on the gas pressure.

- **Aerogel Cherenkov:** Both spectrometers are equipped with a Cherenkov detector that uses an aerogel to distinguish between $p/\pi/K$.
- **Noble Gas Cherenkov (NGC):** The SHMS is equipped with an additional NGC detector that uses either argon, neon, or a mixture of the two gases to distinguish between e/π at momenta above 6 GeV/c.

Each of these detectors contain PMTs to detect the photons emitted as Cherenkov radiation. The analog signal produced is then sent to the Counting Room for signal processing and data collection.

Calorimeters

The electromagnetic (EM) calorimeter in each spectrometer provides a measurement of the projectile particle energy by bringing it to a halt, as well as complementing the Cherenkov detectors in e/π discrimination. Because this is a destructive measurement of the energy, it is located at the end of both detector stacks.

As an electron traverses the calorimeter, it is slowed down (decelerated) by the calorimeter radiator. This causes the electron to radiate a bremsstrahlung photon, which in turn decays into e^+e^- via pair production. The process of bremsstrahlung (German for "braking radiation") and pair production continues to produce a cascade of photons, electrons, and positrons in a chain reaction known as an electromagnetic shower (see Fig. 2.11). The shower continues to develop until most or all the initial electron energy has been deposited in the calorimeter. The total energy deposited is

then read out by PMTs. [14] This signature allows one to differentiate between an electron and a pion.

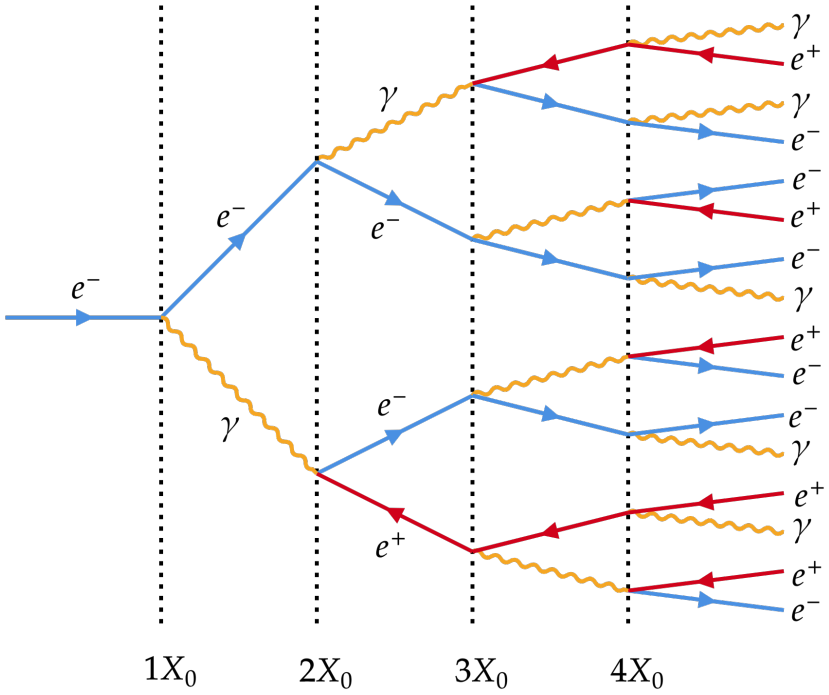

Figure 2.11. The development of an electromagnetic shower in a calorimeter. Note: Redrawn from [13].

2.4 Overview of Experiment E12-10-003

Experiment E12-10-003 at the Thomas Jefferson National Accelerator Facility in Experimental Hall C ran from February 24th, 2023 through March 20th, 2023. The experiment was divided into various groups of runs for specific studies. Each study consisted of a 10.549 GeV electron beam incident on one of the following cryogenic

targets:

- **Liquid Deuterium:** A cryogenic liquid deuterium (LD_2) target for the main experiment involving the $^2H(e,e'p)X$ reaction. The nominal temperature of the liquid was $T_{LD_2} = 22 \pm 0.1$ K at approximately 23 psi (absolute). [14] According to the NIST, at these conditions the density of LD_2 is $\rho_{LD_2} = 0.167$ g/cm^3. [7]
- **Liquid Hydrogen:** A cryogenic liquid hydrogen (LH_2) target for $^1H(e,e')p$ studies. The nominal temperature of the liquid was $T_{LH_2} = 19 \pm 0.1$ K at approximately 25 psi (absolute). [14] According to the NIST, at these conditions the density of LH_2 is $\rho_{LH_2} = 0.0725$ g/cm^3. [7]
- **Aluminum Dummy:** A dummy target consisting of aluminum foils at the cryogenic target entrance and exit windows ($z = \pm 5$ cm) for background subtraction (see Section 3.7). [14]
- **Carbon:** A solid carbon target (^{12}C) used for luminosity studies.

A comprehensive run list of this experiment is given in Table 2.2.

For the main experiment involving the $^2H(e,e'p)X$ reaction, the scattered electron was detected by the SHMS in coincidence with the knocked-out proton detected in the HMS. The SHMS was fixed in angle and central momentum while the HMS angles and central momenta were changed. At these SHMS central momentum and angle values, we expect a four-momentum transfer of $Q^2 = 4.07$ (GeV)^2 [see Eq. (1.8)].

Furthermore, we expect a three-momentum transfer of $q = 2.840$ GeV at an angle $\theta_q = 39.491^\circ$ with respect to the incident electron momentum. The central momentum and angles for the HMS were chosen such that particle X would have a missing momentum corresponding to the respective missing momentum study. At these kinematic settings, contributions from PWBA, FSI, MEC, and IC are suppressed, leaving PWIA as the leading contribution. A simplified Feynman diagram for this reaction under the One Photon Exchange Approximation (OPEA) is shown in Fig. 2.12.

Table 2.2. Run list for Experiment E12-10-003. For each run, the beam energy was set at $E_b = 10.549$ GeV.

Date	Study	Runs	Target	P_{HMS} (GeV/c)	θ_{HMS} (deg)	P_{SHMS} (GeV/c)	θ_{SHMS} (deg)
02/25	^{1}H$(e,e')p$	20840-20844	LH_2	varies	varies	8.55	varies
02/25	Dummy Run	20845	Al	3.499	-33.344	8.55	14.153
02/25-02/26	^{1}H$(e,e')p$	20846-20863	LH_2	varies	varies	8.55	varies
02/26	Dummy Run	20864	Al	1.664	-50.498	8.55	7.704
02/26	^{1}H$(e,e')p$	20865-20870	LH_2	varies	varies	8.55	varies
02/26	120 MeV/c (Set 1)	20871-20872	LD_2	3.0523	-38.63	8.55	12.197
02/26-02/28	580 MeV/c (Set 2)	20873-20883	LD_2	2.2622	-54.96	8.55	12.197
02/28-03/08	800 MeV/c	20886-20956	LD_2	2.1210	-59.39	8.55	12.197
03/08-03/17	900 MeV/c	20958-21048	LD_2	2.0474	-61.33	8.55	12.197
03/17	Lumi	21049-21058	LD_2	2.0474	-61.33	4	20
03/17	Lumi	21059-21063	^{12}C	2.0474	-61.33	4	20
03/17	Lumi	21064	Al	2.0474	-61.33	4	20
03/17-03/18	120 MeV/c (Set 2)	21065-21075	LD_2	3.0523	-38.63	8.55	12.197
03/18-03/20	580 MeV/c (Set 2)	21076-21102	LD_2	2.2622	-54.96	8.55	12.197

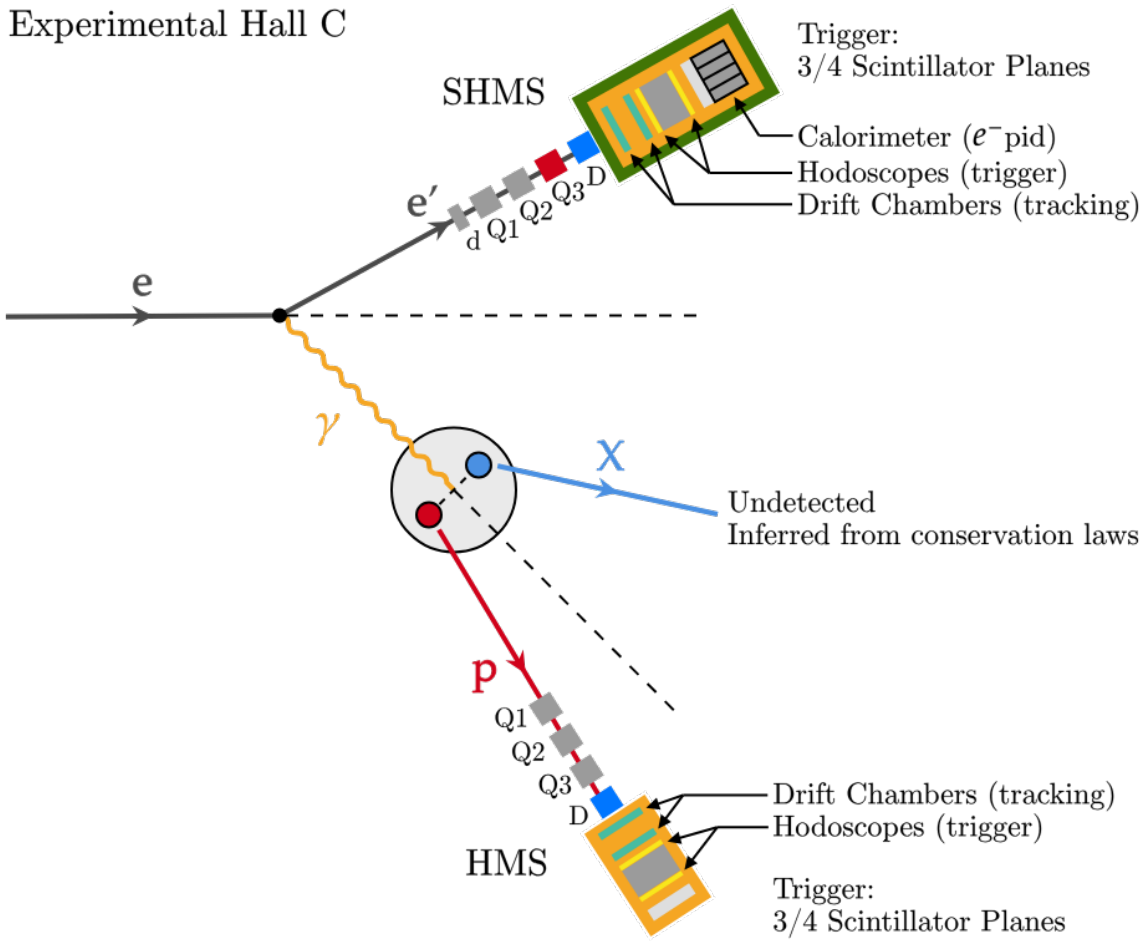

Figure 2.12. Simplified Feynman diagram of the $^2\mathrm{H}(e, e'p)X$ reaction kinematics under the One-Photon Exchange Approximation. Note: Redrawn from Ref. [14]

CHAPTER 3

Data Analysis Overview

3.1 Data Collection and Analysis

Here I discuss how we go from the raw data taken at Hall C to the analyzing process. A flowchart summarizing this process is shown in Figure Fig. 3.1.

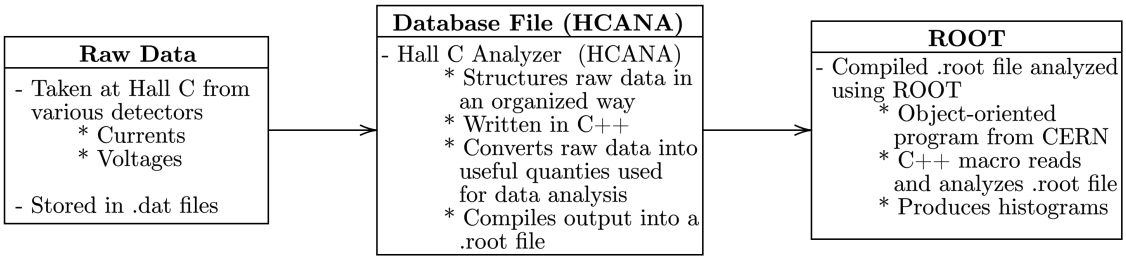

Figure 3.1. Flowchart of data collection and analysis.

3.1.1 Raw Data

The raw data consists of the various currents, voltages, and other electronic signals that were taken by the various detector systems in each spectrometer. The raw data are stored in very large `.dat` files.

3.1.2 Database File

Once the raw data has been stored, it is taken into a database file. The database file used in Hall C is an analyzer written in C++ called HCANA (Hall C Analyzer). The

purpose of the analyzer is to organize the raw data for efficient storage and retrieval, apply various corrections to the raw data, such as timing corrections, and convert the corrected data into useful physical quantities, such as energy and momentum, for data analysis. Furthermore, the analyzer has a tracking algorithm that uses the corrected data to try to reconstruct particle trajectories. The algorithm picks out a "good track" reconstruction based on the criteria it has been set to, which we consider in our data analysis. Once the analyzer is finished, it compiles everything into a `.root` file for data analysis.

3.1.3 ROOT

ROOT is an object-oriented program written in C++ by CERN in 1994 for high energy physics data analysis. The key feature of ROOT is that it uses a *tree* data structure with substructures *branches* and *leaves*. Each branch contains data saved as a `.root` file, and each leaf of a branch produces a histogram that is predetermined by a C++ macro that is written to read through the `.root` file. This structure provides a very efficient method for accessing huge amounts of data [1]. An example of using ROOT is given in Appendix A.

The compiled `.root` files from the analyzer are sent to our research group and are read by various C++ macros that have been written by Dr. Konrad Aniol for our data analysis.

3.2 Target Density Corrections; Boiling Studies

Recall that the luminosity of a particle accelerator is defined by

$$\mathcal{L} \equiv \Gamma_{\text{inc}} n_t \Delta L, \tag{3.1}$$

where Γ_{inc} is the rate of incident particles, n_t is the target density, and ΔL is target chamber thickness. With this definition, we may write the scattering rate as

$$\Gamma_{\text{sct}} = \sigma \mathcal{L}, \tag{3.2}$$

where σ is the cross section. The luminosity measures how many particle collisions occur per unit time and area; that is, it determines the rate of events. As the electron beam presents itself onto the cryogenic targets, it deposits a large amount of heat that may cause localized boiling, which then leads to a reduction in target density and so reduces the amount of interactions we can study. [14] Furthermore, the beam current can vary, and this variation in beam current can also create changes in the target density.

A series of dedicated runs (see Table 3.1) were taken independently in each spectrometer (single-arm) at various beam currents to study target density reductions in Carbon-12 and LD_2. Here we shall be concerned with the data taken by the SHMS. These runs were taken at a spectrometer central angle and momentum settings of 61.33° and 2.0474 GeV/c, respectively, at a beam energy of $E_b = 10.549$ GeV. (These are the same settings as the 900 MeV/c missing momentum settings). This analysis

consists of determining the charge yield as a function of beam current to determine the yield loss with increasing beam current. [14]. In this analysis, two separate charge yields were determined and defined as

$$Y = \frac{N_e}{Q} \tag{3.3}$$

$$Y_{\text{cor}} = \left(\frac{\text{PS2}}{\text{T2} \cdot \epsilon_{\text{strk}}}\right)\frac{N_e}{Q} = \left(\frac{\text{PS2}}{\text{T2} \cdot \epsilon_{\text{strk}}}\right)Y \tag{3.4}$$

where Eq. (3.3) is the yield calculated from the total number of electron counts divided by the total charge and Eq. (3.3) is the yield multiplied by several correction parameters:

- T2 [kHz]: scaler trigger rate
- PS2: pre-scale factor for the T2 trigger
- ϵ_{strk}: tracking efficiency for the SHMS

Uncertainty calculations are shown in Appendix B.

Figures 3.2 and 3.3 show plots of the yield loss versus beam current for Carbon-12 and LD2, respectively. The linear fit function used was

$$Y = m \cdot I_{\text{beam}} + Y_0, \tag{3.5}$$

where Y is the charge yield, I_{beam} is the average beam current, m is the slope, and Y_0 is the y-intercept parameters.

We see that the corrected yield fits the data better that the uncorrected yield, especially for the LD_2 runs. We can determine the reduction in target density by

Table 3.1. Target density reduction study.

Run	Target	N_e	Q (mC)	I (μA)	T2	PS2	ϵ_{strk}
21059	^{12}C	200989	9.864	14.858	1.000	1	0.987
21060	^{12}C	327115	16.041	29.442	1.001	1	0.988
21061	^{12}C	354160	17.301	38.786	1.000	1	0.987
21062	^{12}C	755262	37.089	55.328	1.000	1	0.986
21063	^{12}C	741566	36.660	64.626	0.996	1	0.986
21049	LD_2	181598	5.592	9.965	1.000	1	0.987
21050	LD_2	182231	5.592	14.828	0.998	1	0.986
21051	LD_2	372215	12.140	24.823	0.953	1	0.985
21052	LD_2	237592	14.744	34.051	1.006	2	0.984
21053	LD_2	263496	16.278	38.137	1.006	2	0.983
21054	LD_2	290203	17.998	41.540	1.006	2	0.983
21055	LD_2	494134	30.784	42.459	1.005	2	0.983
21056	LD_2	275132	25.631	51.005	1.014	3	0.981
21057	LD_2	312336	29.647	64.827	0.986	3	0.981
21058	LD_2	375022	36.805	67.364	0.980	3	0.979

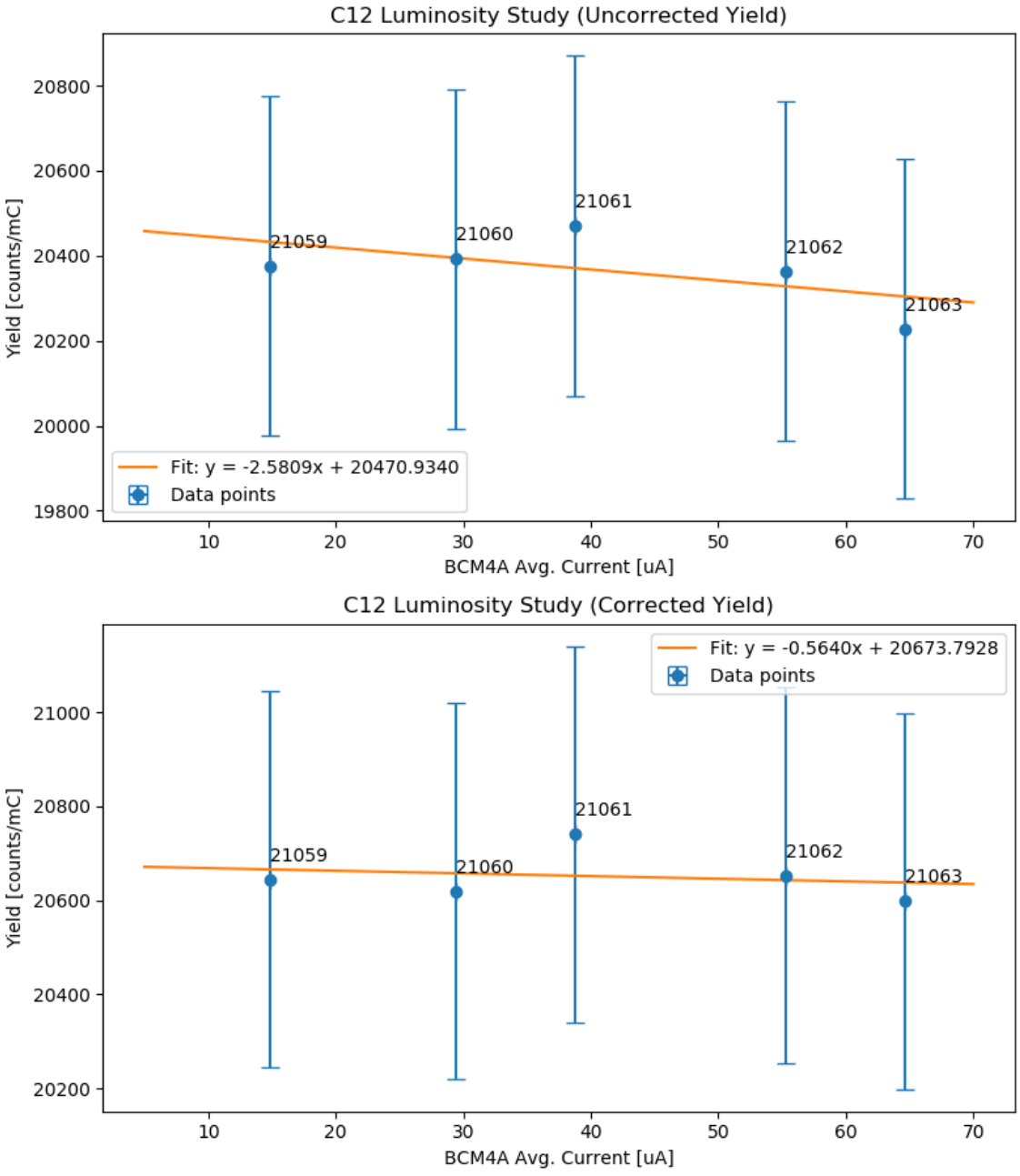

Figure 3.2. Carbon-12 uncorrected (top) and corrected (bottom) charge yields.

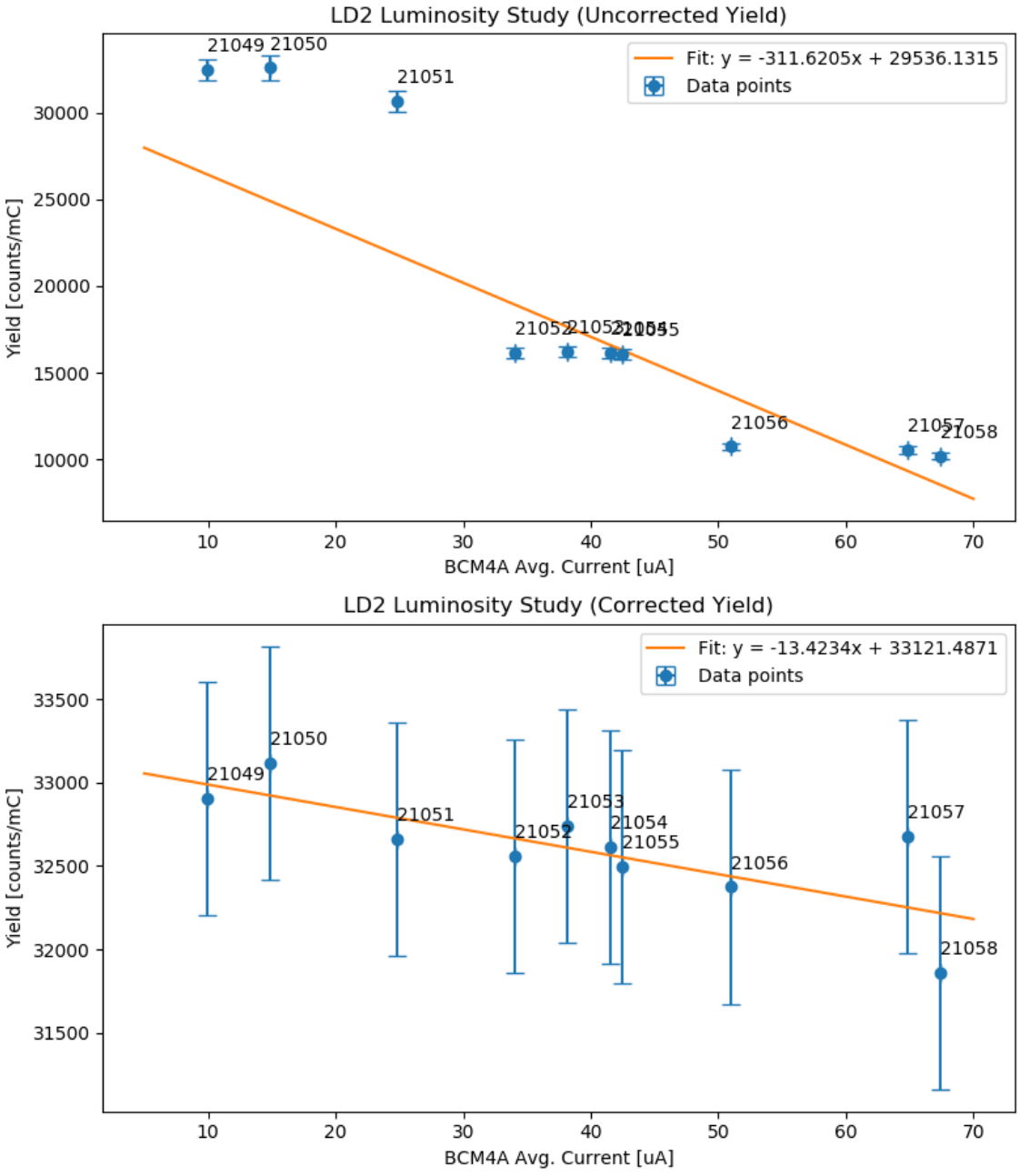

Figure 3.3. LD_2 uncorrected (top) and corrected (bottom) charge yields.

considering the normalized density

$$f(I) = \frac{Y(I)}{Y_0}, \tag{3.6}$$

where $Y(I)$ is the charge yield at some current I and Y_0 is a reference charge yield, which we take to be the yield at zero current. The yield reduction for a given current I is then given by

$$\Delta Y(I) = 1 - f(I). \tag{3.7}$$

We consider the yield reduction from zero current to 70 μA, which is about the maximum current set for both ^{12}C and LD_2. For ^{12}C we find a 0.19% reduction in the charge yield. This almost non-existent reduction in the charge yield is expected for a solid target such as ^{12}C. For LD_2 we find a 2.8% reduction in the charge yield. This is significantly more than for a solid target, but is expected for a cryogenic target.

3.3 Cuts

To ensure that we are selecting only events of interests, namely, the events corresponding to the electro-disintegration reaction, various cuts have to be made to the data. These cuts may be seen as additional selection criteria to the data that are determined based off the analysis of the data. The following sections shall explore some of these analyses and cuts.

3.4 Coincidence Time-of-Flight Cut

The coincidence time-of-flight gives the time difference between the detection of the electron in the SHMS and the detection of the proton in the HMS. Random coincidences are events that originate from anywhere, whereas true coincidences are events that occur from the same vertex. [6] A peak in the coincidence time-of-flight spectrum indicates a true coincidence, that is, that the scattered electron and proton came from the same vertex. This allows us to trace back to the $^2\mathrm{H}(e, e'p)X$ interaction vertex.

Figure 3.4(a) shows a coincidence time-of-flight for the 580 MeV/c missing momentum setting. The sharp peak in this spectrum centered at $t_{\mathrm{peak}} \approx 66.5$ ns indicates a true coincidence. The much smaller periodic peaks occur roughly every 4 ns and corresponds to the pulses of the CEBAF accelerator. This background was subtracted off by placing a coincident time cut in the range $65.0 < t_{\mathrm{coin}} < 68.2$ for each kinematic setting. A spectrum of the coincide time-of-flight after making this cut is show in Fig. 3.4(b). This same coincidence time cut was placed for the other missing momentum settings.

3.5 Spectrometer Aperture Cuts

Our C++ macro allows us to specify the percentage of the central HMS aperture to be used. This effectively limits the possible ranges of protons going into the HMS, which in turn limits the amount of *ep* coincidences. It was recommended by our

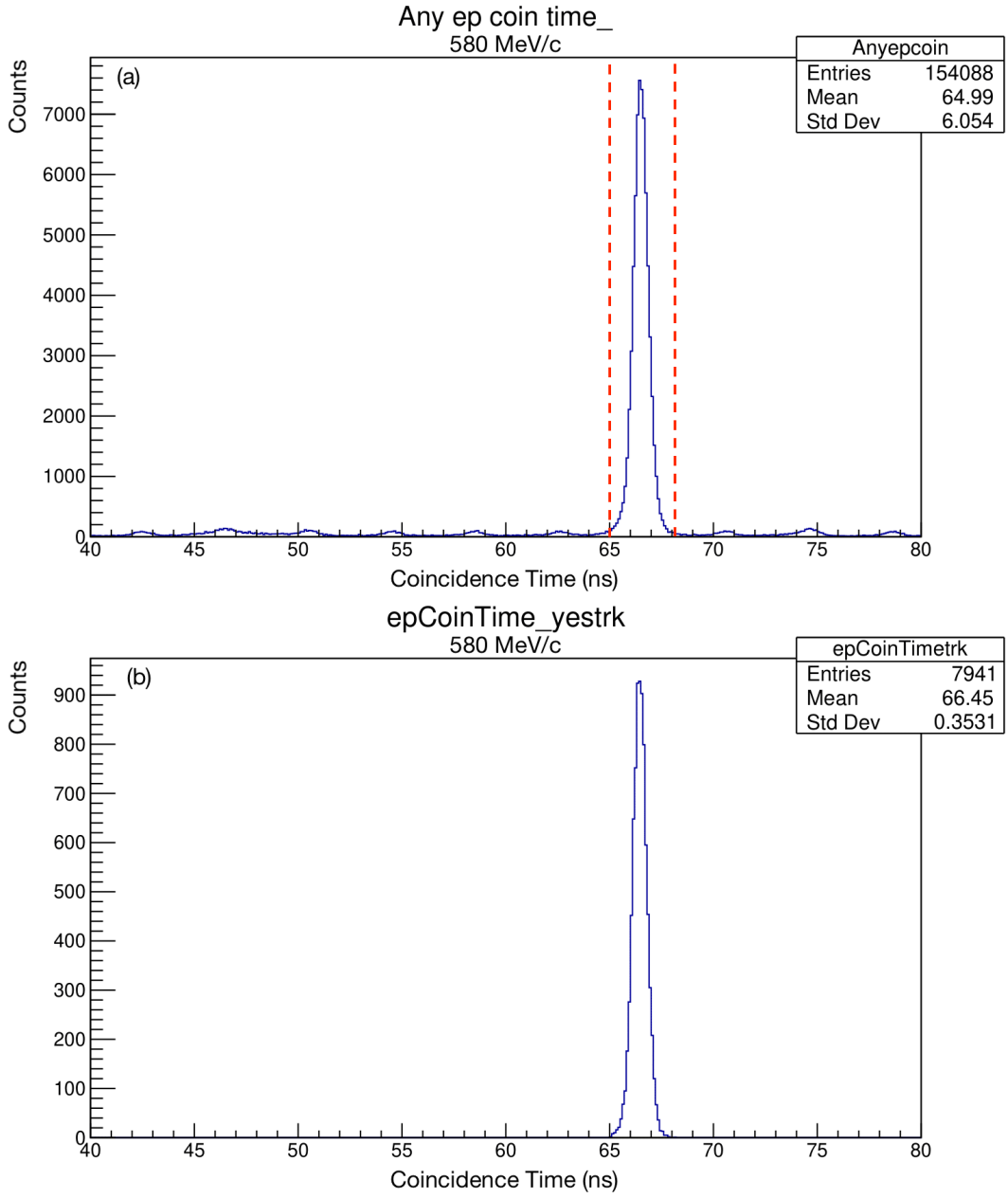

Figure 3.4. Coincidence time-of-flight spectrum for the 580 MeV/c missing momentum setting (a) before and (b) after placing the coincidence time cut, $65.0 < t_{\text{coin}} < 68.2$. These same cuts were also placed for the other missing momentum settings.

Jefferson Lab colleague, Dr. Mark Jones, to use an 8% aperture cut.

3.6 Angle Cuts

For each missing momentum setting, we the following angle cuts were made on the scattered electron and knocked-out proton:

- $\theta_e = \pm 0.03$ rad.
- $\phi_e = \pm 0.016$ rad.
- $\theta_p = \pm 0.06$ rad.
- $\phi_p = -0.01$ to $+0.03$ rad.

3.7 Target Chamber Background Subtraction

Although the *ep* coincidence time tells us that the electron and proton came from the same interaction vertex, it does not say specifically which interaction it came from. Of course, we expect these coincidences to originate from the deuteron electrodisintegration interaction vertex. However, there may be additional unwanted interactions that need to be accounted for. In particular, we must consider any possible interactions with the aluminum target chamber. After all, we are not only bombarding the deuteron targets with electrons but also the aluminum target chamber itself.

Ideally, this issue can be resolved by performing runs at each missing momentum setting with just the aluminum target chamber alone; that is, with no gas inside.

Any interaction events that are counted from these "dummy runs" could then be subtracted off from the respective deuteron runs. However, these runs were not taken for any of the missing momentum settings, as previous experiments and reports have found that dummy contributions were negligible.

3.7.1 LH_2 Aluminum Dummy Run Analysis

Despite not having any dummy runs taken for the main LD_2 experiments, two dummy runs were taken in the LH_2 experiment: Run 20845 and Run 20864 (see Table 2.2). Figure 3.5 shows the proton count spectrum for Run 20845 from $z = \pm 10$. Specifically, Fig. 3.5(a) shows proton production from the aluminum target chamber for any *ep* coincidence, and Fig. 3.5(b) shows proton production from the aluminum target chamber after selecting the protons that meet the good track reconstruction criteria. In both plots, we see a sharp peak located around $z = -5$ cm and $z = +5$ cm, which corresponds to the target chamber's entrance and exit windows, respectively. We see that most proton production from the aluminum target chamber occurs at the entrance and exit windows, with very little to no proton production in-between the target chamber. This is especially true with the good track criteria, in which the proton production is significantly less.

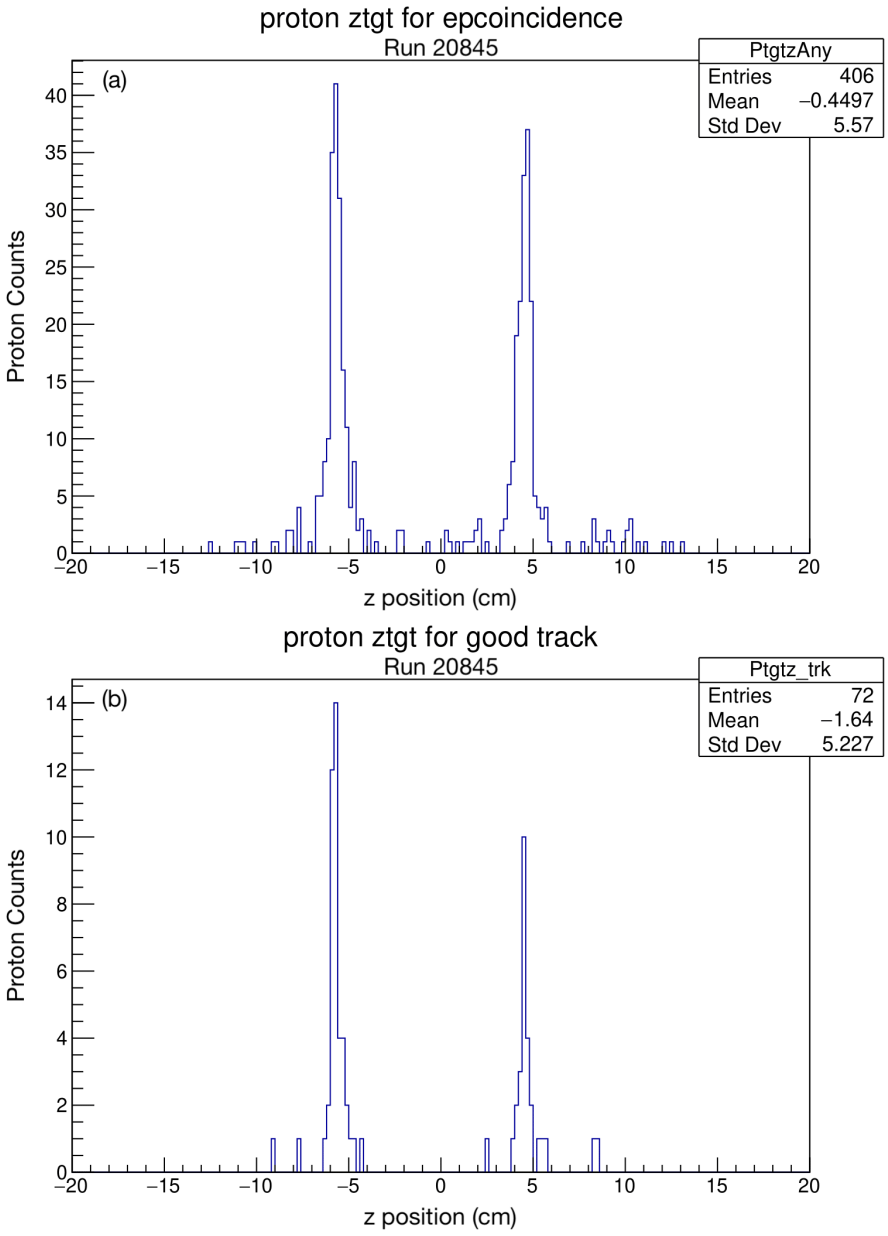

Figure 3.5. Proton count spectrum of an Aluminum dummy run (a) for any *ep* coincidence and (b) for good track reconstruction, using a $z = \pm 10$ cm cut.

3.7.2 LD_2 Proton Production Analysis

Although we do not have dummy runs for the main LD_2 experiment, we may still explore the proton count spectrum for each missing momentum setting. Figure 3.6 shows such plots from $z = \pm 10$ with the good track criteria imposed. It is interesting to note that the 580, 800, and 900 MeV/c settings have the same structure, namely, a sharp peak at $z = \pm 5$ cm and a decline in proton production with increasing z position. The 120 MeV/c setting, on the other hand, does not have the sharp peaks and has a much larger decline in proton production with increasing z position. A quadratic fit of the proton counts for the 120 MeV/c setting is shown in Fig. 3.7.

Current research is on-going in explaining this downward flow of proton production. One such explanation may be facilitated via the fluid dynamics in the target loop (see Fig. 2.4). The cryogenic LD_2 enters and exits at the upstream end of the target cell, whereas there are no outlets for the fluid at the downstream end of the target cell. A Computational Fluid Dynamics (CFD) simulation was done by Dr. Silviu Dusa of Jefferson Lab and is shown in Fig. 3.8. Note that the target cell is reversed in this simulation, as indicated in the figure. This simulation indicates that there is a loss of target density from the upstream to the downstream end of the target chamber, resulting in about a 6.00% loss in the target density. Our proton production plots in Figure 3.6, however, seem to indicate a much higher loss in target density.

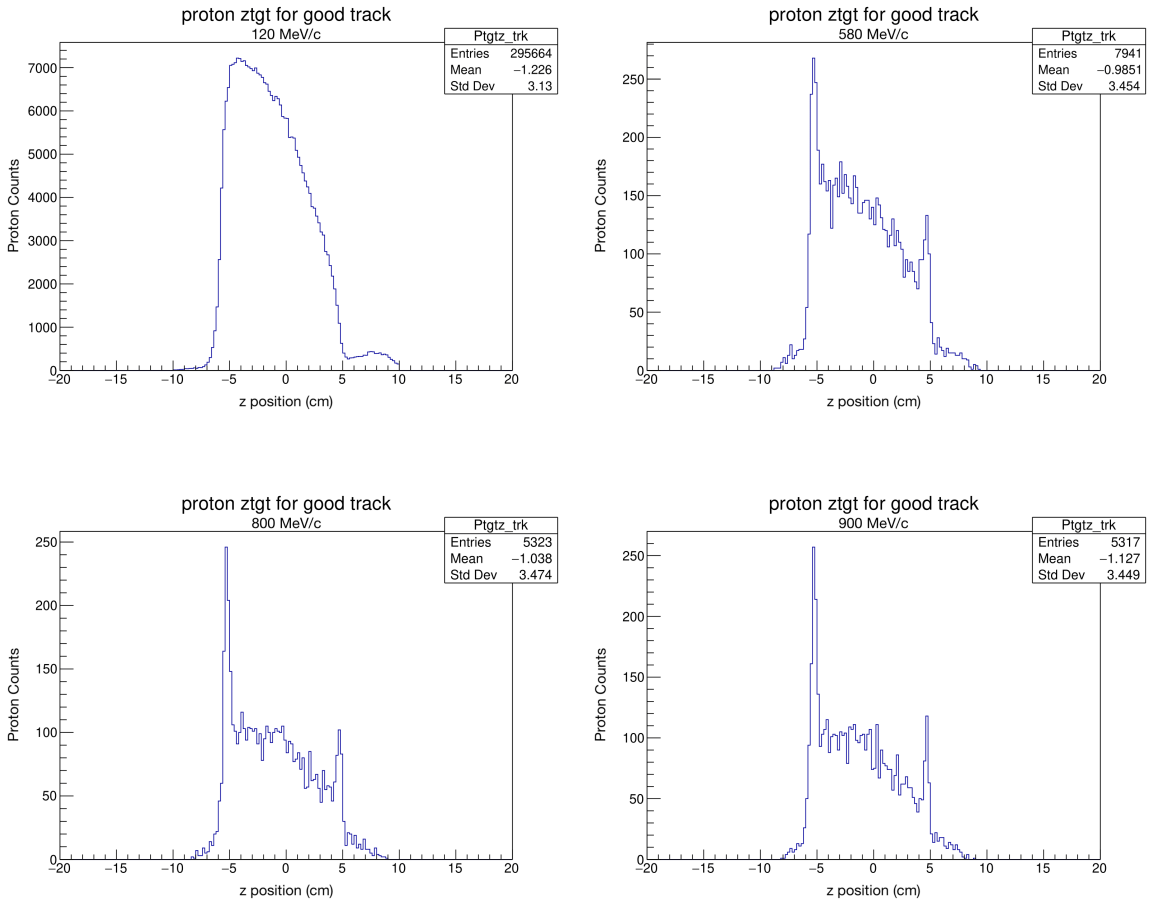

Figure 3.6. Proton count spectrum of each LD_2 missing momentum setting using a $z = \pm 10$ cm cut.

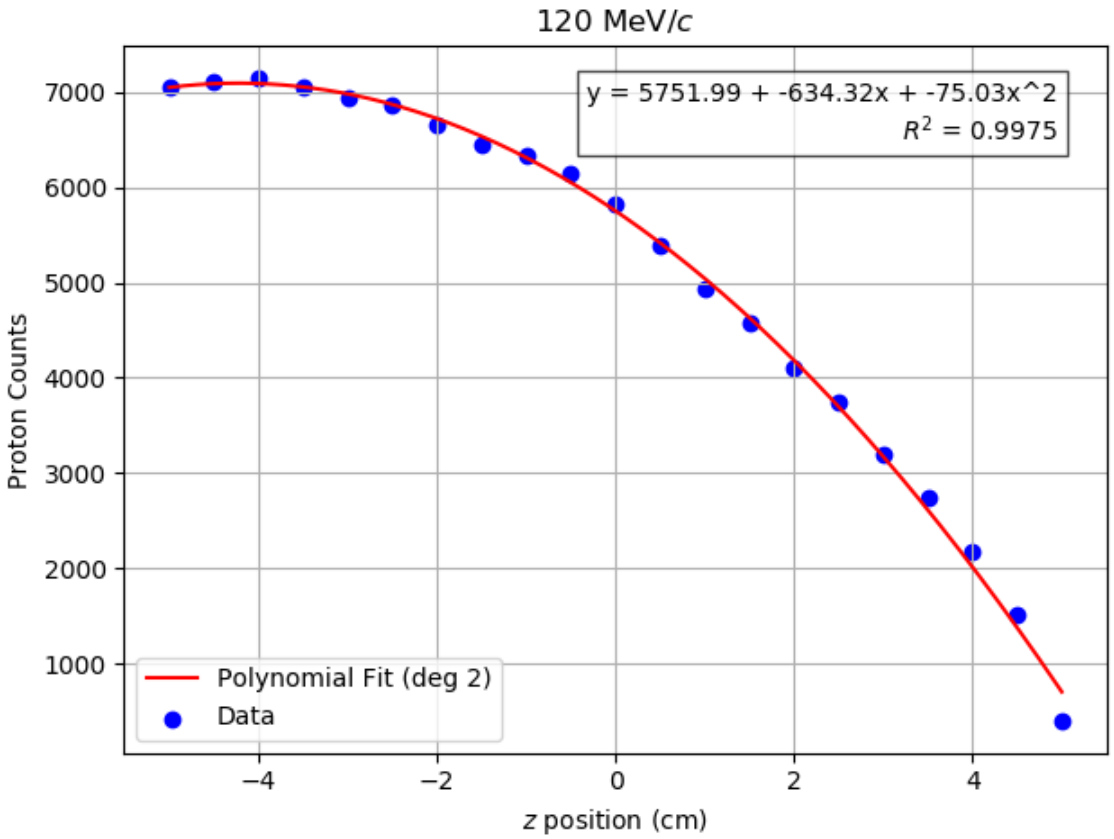

Figure 3.7. A quadratic fit of the proton counts for the 120 MeV/c setting within the target chamber ($z = \pm 5$ cm) width.

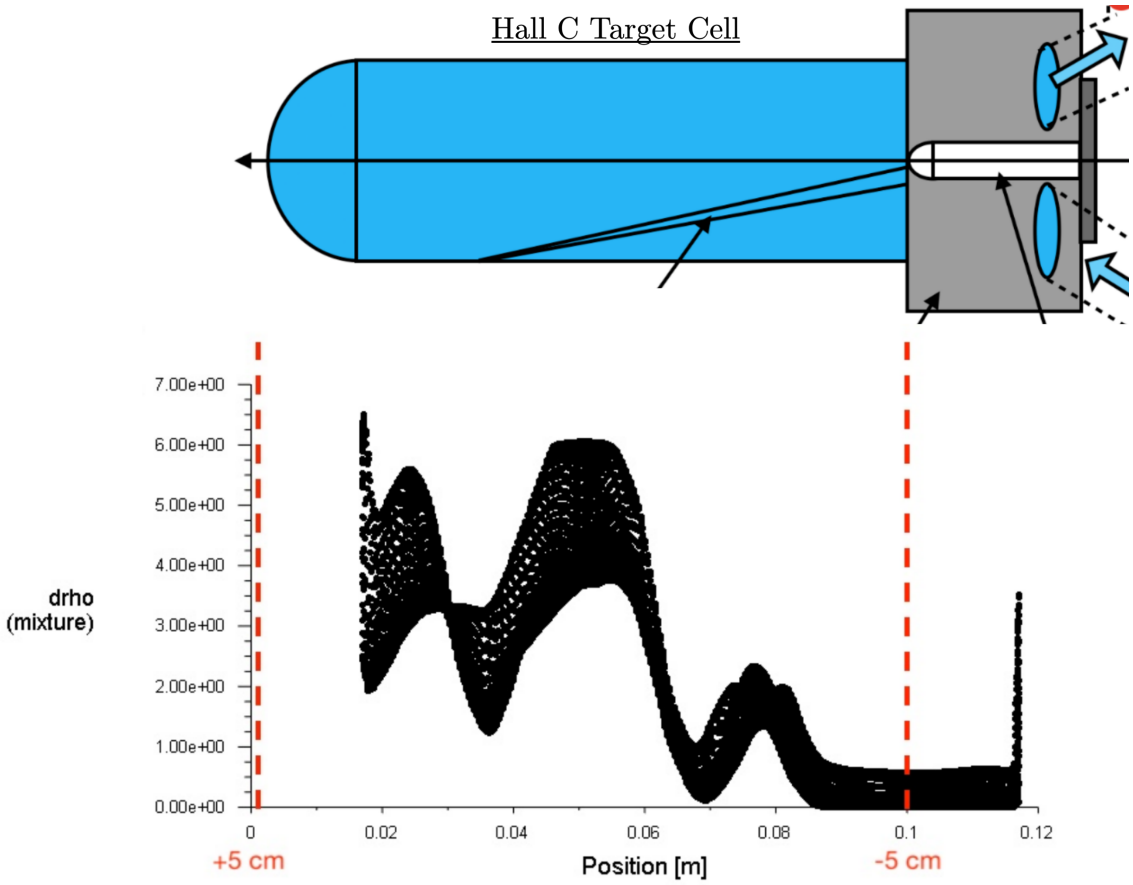

Figure 3.8. Computational Fluid Dynamics (CFD) simulation showing loss of target density with position.

It is interesting to note that the proton counts per cm is approximately constant for each kinematic setting. Table 3.2 summarizes this. For each kinematic setting, the total number of protons between a given target region was counted. By dividing out this number by the length of the region, we obtain the number of protons per cm within that region. These values are in close agreement with each of the target regions in the respective kinematic setting.

Table 3.2. Proton Production Counts

Kinematic Setting	Target Region	Proton Counts	Proton Counts per cm
120 MeV/c	±4 cm	198098	24762
	±3 cm	158491	26415
	±2 cm	109462	27365
	±1 cm	56083	28041
580 MeV/c	±4 cm	4435	554
	±3 cm	3587	598
	±2 cm	2450	612
	±1 cm	1261	630
800 MeV/c	±4 cm	2863	358
	±3 cm	2281	380
	±2 cm	1591	398
	±1 cm	834	417
900 MeV/c	±4 cm	2809	351
	±3 cm	2271	379
	±2 cm	1564	391
	±1 cm	798	399

3.7.3 Target Cell Length Cut

From our above analysis, we conclude that unwanted proton production resulting from the electron beam interacting with the aluminum target chamber itself predominantly occurs at the target cell's entrance and exit windows, with very little to none occurring inside the target chamber. Although our analysis and previous experiments have shown that these effects are negligible, we wish to stay away from the entrance and exit windows, where most of these unwanted interactions occur. Thus, a $z = \pm 4$ cm target cell length cut was placed for each missing momentum setting.

CHAPTER 4

Extraction of Deuteron Cross Section

4.1 The Experimental $^2\mathbf{H}(e, e'p)X$ Cross Section

The kinematic variables of interest in this experiment are the angular distributions of the scattered proton and electron, as well as the energy distribution of the scattered electron. The total cross section for the $^2\mathrm{H}(e, e'p)X$ reaction is given by

$$\sigma = \frac{N_d}{\Delta\Omega_e \Delta\Omega_p \Delta E_e N_e N_{\mathrm{tgt}}} \cdot \left(\frac{\mathrm{RSC}}{\mathrm{Eff}}\right), \tag{4.1}$$

where we have the following (see Table 4.2):

- N_d is the total number of deuterons that have been disintegrated. This is equivalent to the number of protons, since each proton corresponds to a deuteron that has been disintegrated. These values can be found from the missing mass plots (see Fig. 4.2).
- $\Delta\Omega_e$ and $\Delta\Omega_p$ are the geometrical solid angles of the spectrometer apertures. These are found by the expression $\Delta\Omega = \sin|\theta|\Delta\theta\Delta\phi$, where θ is the spectrometer central angle, $\Delta\theta$ is the width of the θ cut, and $\Delta\phi$ is the width of the ϕ cut. Note that we take the absolute value of spectrometer central angle; this is to ensure that the solid angle, and, therefore, the total cross section, comes out positive.

- ΔE_e is the energy width of the scattered electrons taken into consideration.
- $N_e = Q/e$ is the number of electrons that passed through the target, where e is the electron charge and Q is the total accumulated charge.
- $N_{\text{tgt}} = \rho(I) z_{\text{tgt}}/m_d$ is the number of deuterons per cm^2 in the beam, where I is the beam current, $\rho(I)$ is the number of deuterons per cm^3, $m_d = 3.371 \times 10^{-24}$ g is the mass of the deuteron, and z_{tgt} is the cut on the target length, which we took to be 8 cm.

In addition to these quantities, we also have the following correction and efficiency factors that must be taken into account when calculating the cross section (see [6] and [3]):

- RSC is the radiative and straggling corrections to the cross section due to the tail on the electron spectrum. This takes into account the fact that we consider all scattered electrons, even those that have been radiated.
- Eff is the efficiency factor and it accounts for the following detector and signal parameters:
  (1) data acquisition live time (LTdaq)
  (2) electronics live time (LTel)
  (3) trigger efficiency (Tri)
  (4) wire chamber (WC)

(5) tracking efficiencies (Tra)

The efficiency factor is given by

$$\text{Eff} = \text{LTd} \cdot \text{LTe} \cdot \text{Tri} \cdot \text{WC} \cdot \text{Tra}. \tag{4.2}$$

4.2 Missing Momentum Ratio

Although HCANA does a calculation of the missing momentum, our C++ macro takes in the necessary data from HCANA to also perform a calculation of the missing momentum. This serves as a cross check between HCANA's calculation and our calculation. We define `pmisstot` to be our calculation of the missing momentum and `pmiss` as HCANA's calculation. If the calculation of the missing momentum has been done correctly, then the ratio `pmisstot/pmiss` should be equal to unity.

A histogram for the ratio `pmisstot/pmiss` was created for each missing momentum setting (Fig. 4.1). For the 580, 800, and 900 MeV/c setting, we see a sharp peak centered at unity, indicating that the missing momentum calculation by HCANA and our C++ macro are in agreement. However, for the 120 MeV/c setting this peak is not as sharp. There is quite a large broadening at the base of the peak, which indicates that there is some sort of disagreement with the HCANA calculation and our C++ macro calculation for this setting. Since our C++ macro remains exactly the same for each setting, it is possible that there may be something wrong with how HCANA is producing its calculation for the 120 MeV/c data, an issue that we

presented to our colleagues for them to look into and resolve.

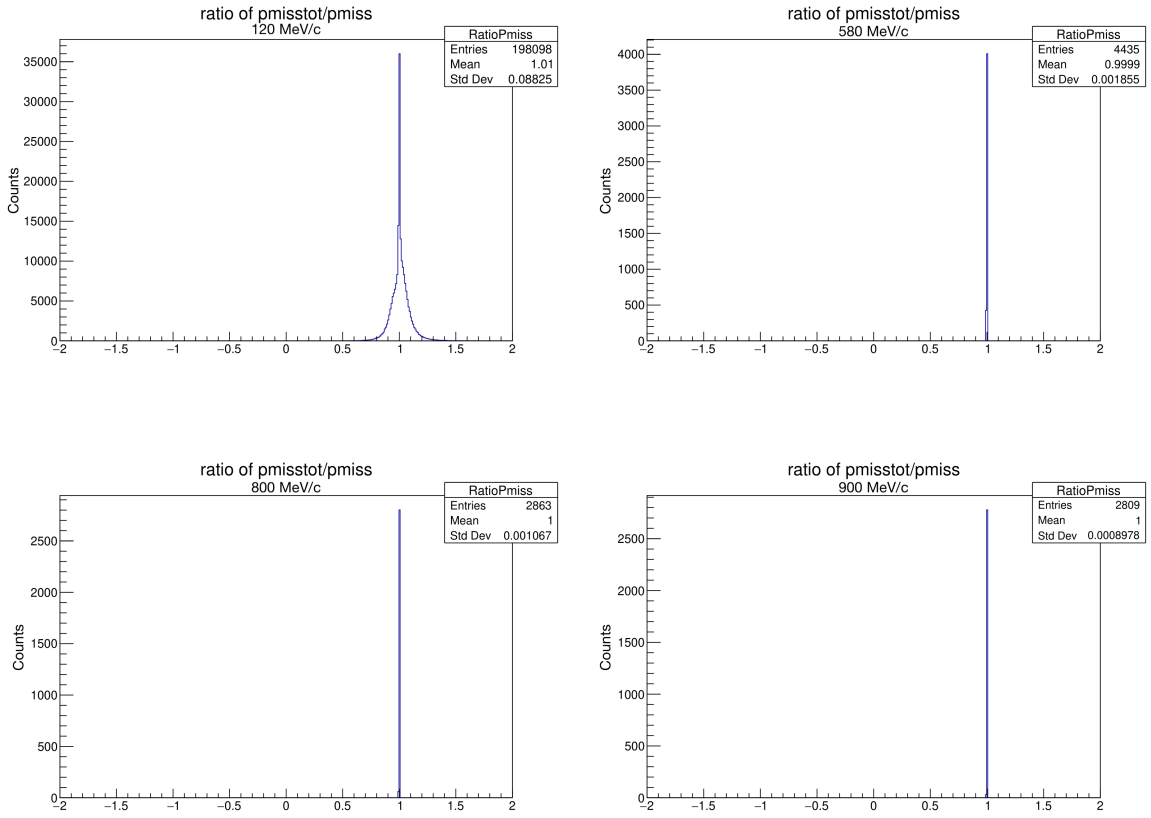

Figure 4.1. Histogram of calculated missing momentum ratio for each missing momentum setting.

4.3 Missing Mass

Our C++ macro performs a calculation of the missing mass as defined in Eq. (1.16) for each missing momentum setting. These histograms are shown in Fig. 4.2.

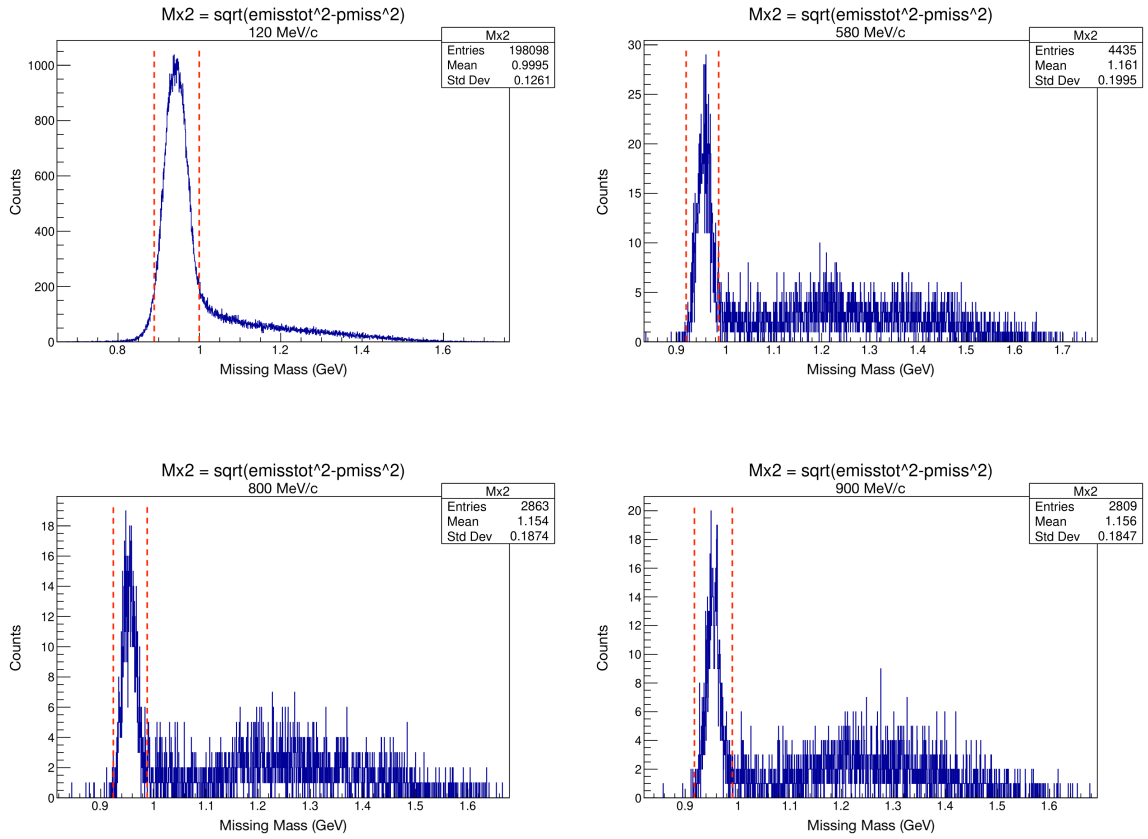

Figure 4.2. Histogram of calculated missing mass for each missing momentum setting.

We can see from the entries count that there were significantly more events for the 120 MeV/c setting than for the other settings. In other words, there were much more protons (or deuteron disintegrations) at this setting than for the others. Thus, the 120 MeV/c provides the most sharpest and cleanest histogram. In each setting, we find a sharp peak in the missing mass region between 0.9 to 1.0 GeV. Since the mass of the neutron is taken to be 0.939 GeV, we may conclude that these sharp peaks correspond to the neutron. Table 4.1 shows the percent difference between the average missing mass between this region to the accepted value of the neutron mass for each setting.

Table 4.1. Percent Difference of Average Missing Mass in the Region $0.9 - 1.0$ GeV.

Missing Momentum Setting	Average Missing Mass (GeV)	Percent Difference
120 MeV/c	0.945	0.64%
580 MeV/c	0.958	2.02%
800 MeV/c	0.957	1.92%
900 MeV/c	0.955	1.70%

The "residual tail" that extends to higher missing momentum can arise from various sources, including the following:

- **Final State Interactions:** The ejected proton and recoiling neutron may have continued to interact further despite our efforts to minimize this effect. This can distort the kinematics of the detected proton, leading to misconstruction of the missing mass.

- **Radiative Effects:** The electrons may have been radiated via Bremsstrahlung, distorting the initial state energy and again leading to misconstruction of the missing mass.

4.4 Total Cross Section

We summarize the data collected for extracting the total cross section in Table 4.2. In obtaining the total cross section for each missing momentum setting, the target density corrections were not applied. Rather, the nominal density of the liquid deuterium ($\rho_{\mathrm{LD}_2} = 0.167$ g/cm^3) was used. Thus, $N_{\mathrm{tgt}} = 3.96 \times 10^{23}$ cm^{-2}. Additionally, we made the approximation that RSC/Eff = 1. Table 4.3 summarizes the (uncorrected) total cross sections that were found for each missing momentum setting.

Table 4.2. Total cross section extraction data. For each setting, $\Delta\Omega_e = 4.06 \times 10^{-4}$ sr.

Kinematic Setting	Q (mC)	N_e	N_d (or N_p)	$\Delta\Omega_p$ (sr)	ΔE_e (GeV)
120 MeV/c	844.231	5.270×10^{18}	198098	3.00×10^{-3}	1.32
580 MeV/c	9946.684	6.209×10^{19}	4435	3.93×10^{-3}	1.82
800 MeV/c	23421.214	1.462×10^{20}	2863	4.13×10^{-3}	1.86
900 MeV/c	21223.632	1.325×10^{20}	2809	4.21×10^{-3}	1.89

Table 4.3. Total Cross Section for Each Missing Momentum Setting (Uncorrected)

Kinematic Setting	σ ($cm^2/sr^2 \cdot$ GeV)
120 MeV/c	5.90×10^{-32}
580 MeV/c	6.21×10^{-35}
800 MeV/c	1.59×10^{-35}
900 MeV/c	1.69×10^{-35}

CHAPTER 5

Conclusion and Future Studies

A reduction in the charge yield with increasing beam current was found for liquid deuterium. The proton counts as a function of z-target was found to have a downward flow, indicating a change in target density from the upstream to the downstream end of the target cell. Further research needs to be done to determine the cause of this issue. Electron scattering from the aluminum target chamber was determined to be negligible, but precautions were taken by considering a target chamber cut away from the walls. For each missing momentum setting, a neutron was found to be contained in the missing mass spectrum. The residual tail extending to higher missing momentum may be due to various interactions and/or radiative loses that have distorted and therefore led to a misconstruction of the missing mass.

Extracting the cross section of the deuteron and comparing with theoretical models is currently ongoing in our research group. Particularly, we must determine the RSC and Eff factors, as well as taking into account target density corrections due to heat and variation of the electron beam. Furthermore, uncertainties for each of the quantities in the cross section have to be taken into consideration.

REFERENCES

[1] CERN. Root: Data analysis framework. Accessed: January 10, 2025.

[2] Boeglin, W. U. et al. Probing the high momentum component of the deuteron at high Q^2. *Phys. Rev. Lett.*, 107:262501, Dec 2011.

[3] Iqbal, S. et al. Probing for high-momentum protons in ^{4}He via the $^4\mathrm{He}(e, e^{'}p)x$ reactions. *Phys. Rev. C*, 105:064003, Jun 2022.

[4] M. Garçon and J. W. Van Orden. *The Deuteron: Structure and Form Factors*, page 293–378. Springer US, 2001.

[5] H. F. Ibrahim. The $^2\mathrm{H}(e, e'p)n$ reaction at high four-momentum transfer, 2006.

[6] S. Iqbal. Study of $^4\mathrm{He}(e, e'p)^3\mathrm{He}$ through the $(e, e'p)$ reaction at $q^2 = 2$ $(\mathrm{gev}/c)^2$ and $x_b = 1.24.$, 2013.

[7] Eric W. Lemmon, Ian H. Bell, Marcia L. Huber, and Mark O. McLinden. *Thermophysical Properties of Fluid Systems*. National Institute of Standards and Technology, Gaithersburg, MD, 2025. Retrieved: April 19, 2025.

[8] R. Lietava. Introduction to triggering. Accessed: March 31, 2025.

[9] M. Naghdi. Nucleon-nucleon interaction: A typical/concise review. *Physics of Particles and Nuclei*, 2014.

[10] D. H. Perkins. *Introduction to High Energy Physics*. Cambridge University Press, Cambridge, 4th edition, 2000.

[11] J. R. Taylor. *An Introduction to Error Analysis*. University Science Books, 2nd edition, 1997.

[12] J. R. Taylor. *Classical Mechanics*. University Science Books, 2005.

[13] M. Thomson. *Modern Particle Physics*. Cambridge University Press, Cambridge, 2013.

[14] C. Yero. Cross section measurements of deuteron electro-disintegration at very high recoil momenta and large 4-momentum transfers (q^2), 2020.

APPENDIX A

ROOT Replay Example

(1) Open ROOT using the `root` command.

(2) Once ROOT has been initialized, enter the following commands to begin the run process:

```
.x chainit.C2("file name");
```

```
.x nuts.C
```

The first commands tells ROOT which `.root` files to replay, and the second command executes the C++ macro you wish to read into the `.root` files.

(3) Once ROOT has completed the run, quit and exit the program using the `.q` command.

(4) To view the ROOT file completed for data analysis, open ROOT again using the `root` command. Enter `TBrowser B;` to view the histograms of the ROOT file.

APPENDIX B

Target Density Corrections Uncertainty Calculations

"A conservative estimate of the relative uncertainty on the BCM4A charge and on the number of electrons was determined to be $\delta Q/Q = 0.02$ and $\delta N_e/N_e = 0.005$, respectively" [14].

For the uncorrected data, we have

$$Y = \frac{N_e}{Q}.$$

Using the rules of propagation of uncertainties [11], we find

$$\delta Y = \frac{N_e}{Q}\sqrt{\left(\frac{\delta N_e}{N_e}\right)^2 + \left(\frac{\delta Q}{Q}\right)^2}. \tag{B.1}$$

For the corrected data we have

$$Y_{\text{cor}} = \left(\frac{\text{PS2}}{\text{T2}\cdot\epsilon_{\text{strk}}}\right)\frac{N_e}{Q}.$$

Assuming these corrections factors to be exact numbers, we find for the uncertainty

$$\delta Y_{\text{cor}} = \frac{\text{PS2}}{\text{T2}\cdot\epsilon_{\text{strk}}}\frac{N_e}{Q}\sqrt{\left(\frac{\delta N_e}{N_e}\right)^2 + \left(\frac{\delta Q}{Q}\right)^2}. \tag{B.2}$$

APPENDIX C

Data Directories

For this research project, I used the computer "Typhoon" in Dr. Aniol's office. Here I list my directories in case one would need to access any data or results:

- My home directory: `/home/love`
- My data directory: `/home/love/data`

Here you will find various directories corresponding to their respective kinematic study. Each directory contains compiled `.root` files from the analyzer, C++ macros to read these files, and the produced `.root` files from ROOT.